Observing and Modeling the Optical Counterparts of Short-Period Binary Millisecond Pulsars.

Joshua Schroeder

Submitted in partial fulfillment of the
requirements for the degree
of Doctor of Philosophy
in the Graduate School of Arts and Sciences

COLUMBIA UNIVERSITY

2014

ABSTRACT

Observing and Modeling the Optical Counterparts of Short-Period Binary Millisecond Pulsars.

Joshua Schroeder

In this dissertation, I explore the subject of short-period binary millisecond pulsars discovered by the *Fermi Gamma-ray Space Telescope* and radio follow-up teams, and present observations of fields containing eight recently discovered short-period ($P_{\rm orb} <$ 1 d) binary millisecond pulsars using the telescopes at MDM Observatory. The goal of these observations was to detect the optical counterparts of the binaries and, for the best-suited counterparts detected, to observe the photometric variation of the companion that happens over the course of the orbit in various filters. The hope was to then use the light curves to model the systems and obtain constraints on the mass of the neutron stars which are likely to be some of the most massive neutron stars in the galaxy. Optical counterparts to four of these systems are detected, one of which, PSR J2214+3000, is a novel detection. Additionally, I present the fully orbital phase-resolved B, V, and R light curves of the optical counterparts to two objects, PSR J1810+1744 and PSR J2215+5135, for which I employ the ELC model of Orosz & Hauschildt (2000) to measure the unknown system parameters. For PSR J1810+1744 I find that the system parameters cannot be fit even assuming that 100% of the spin-down luminosity of the pulsar is irradiating the secondary, and so radial velocity measurements of this object will be required for the complete solution. However, PSR J2215+5135 exhibits light curves that are extremely well constrained using the ELC model and we find that the mass of the neutron star is constrained

by these and the radio observations to be $M_{\rm NS} > 1.75 M_{\odot}$ at the 3σ level. I also find a discrepancy between the model temperature and the measured colors of this object which I interpret as possible evidence for an additional high-temperature source such as a quiescent disk. Given this and the fact that PSR J2215+5135 contains a relatively high mass companion ($M_{\rm c} > 0.1 M_{\odot}$), I propose that similar to the binary pulsar systems PSR J1023+0038 and IGR J18245-2452, the pulsar may transition between accretion- and rotation-powered modes.

Table of Contents

List of Figures

List of Tables

Acknowledgments

Now I turn to the typical matter task of thanking all those who through various means enabled me to finish this work. I would not have had the opportunity to conduct this research if it were not for the fateful decisions of my parents to procreate, and for the opportunity to explore throughout my life, I am grateful. I also acknowledge the incredible patience and support offered by my partner, Catherine Tan. Members of the Columbia University Astronomy Department have been incredibly supportive even as I struggled to find my way. My Predoctoral Fellowship Advisor at the Harvard-Smithsonian Center for Astrophyics, Dr. Saeqa Vrtilek, has been a gracious host while I've completed my studies at the Harvard-Smithsonian Center for Astrophysics. I also thank Jerry Orsoz, Mark Reynolds, and Robin Barnard for helpful discussions and suggestions directly relevant to this project.

The person who has had the most influence in directing, encouraging, and keeping me moving in the right direction as this dissertation has developed is my advisor, Professor Jules Halpern. I am deeply indebted to his kindness and advising.

To Wit, This is It.

Chapter 1

Background

My dissertation is an exploration of radio-eclipsing, short-period binary millisecond pulsars that are lately being rapidly discovered in increasing number. These objects serve as examples of the unique (astro)physics associated with rapidly spinning neutron stars in binary systems. In this inaugural chapter, I outline the context, history, and work that others have done in exploring such systems as a means to provide a motivation for my dissertation research. The chapter consists of a brief overview of the background necessary for this study, specifically the history of scientific investigations of millisecond pulsars, the extant explanations for their formation and evolution as binary systems, and the relevant observational and theoretical aspects including considerations of the implications of the current proliferation of the discovery of such systems.

Neutron stars have been proposed as a likely product of supernovae since 1934 (Baade & Zwicky, 1934) and have been associated with pulsars since their discovery in 1967 (Hewish et al., 1968; Pilkington et al., 1968; Gold, 1968). The basic model is that the core collapse in a $M \geq 10 M_{\odot}$ should result in a nuclear density object as the compressed mass exceeds the Chandrasekhar mass $M \sim 1.4\ M_{\odot}$. Further, such neutron stars will act as rapidly spinning magnetic dipoles owing to straightforward

arguments from angular momentum and magnetic flux conservation which imply that pulsars are born with short periods ($P < 0.1$ s) and fairly large magnetic fields ($B \sim 10^{12}$ G). The fast rotation at birth produces magnetic dipole radiation that results in energy loss and is associated with large period derivatives ($\dot{P} > 10^{-15}$ s s^{-1}), and, as they spin down, their characteristic ages are given by

$$\tau_c \equiv P/2\dot{P}. \tag{1.1}$$

Meanwhile, the inferred surface magnetic fields assuming typical values for neutron star moments of inertia and radii,

$$B_S \approx 3.2 \times 10^{19} \sqrt{\frac{P\dot{P}}{\mathrm{s}}}\ \mathrm{G}, \tag{1.2}$$

either remain constant or decrease. The youngest pulsars known to exist due to their association with supernovae remnants have periods on the order of 10 ms (Gotthelf et al., 2000) with magnetic fields exceeding $B_S > 10^{11}$ G (Ramanamurthy et al., 1995). In contrast, as a separate class of objects, the so-called "millisecond pulsars" have characteristics that at first blush seem to defy this standard picture of pulsar formation and evolution. The first such object discovered, PSR B1937+21, was discovered in 1982 and was immediately recognized as requiring an alternate formation mechanism owing to its short $P = 1.6$ ms period and small $\dot{P} < 10^{-17}$ s s^{-1} period derivative which implies surface magnetic fields smaller than $B_S <$ few $\times 10^9$ G (Backer et al., 1982). Since then, on order of $\sim 10^2$ such objects have been identified with periods as low as 1.4 ms (Manchester et al., 2005).

Pulsars are visible across the entire electromagnetic spectrum with the Crab Pulsar detected optically shortly after its identification as a pulsating radio source (Cocke et al., 1969). High-energy detections of pulsars began with the identification of Crab X-ray pulsations by Bradt et al. (1969), followed by the discovery of Centaurus X-3

as the first confirmed pulsar identified only in the X-rays (Giacconi et al., 1971), while Geminga is famously the first gamma-ray pulsar without a radio counterpart (Halpern & Holt, 1992). Together with the pulsar winds (as seen, for example, in the energy budget of the Crab Nebula), the high-energy emission – especially in the gamma-rays – is often a significant fraction of the energy available due to the dipole radiation associated with spin-down

$$\dot{E} \approx 3.95 \times 10^{46} \dot{P} \left(\frac{P}{\mathrm{s}} \right)^{-3} \ \mathrm{erg\ s^{-1}}. \tag{1.3}$$

in contrast, radio emission from pulsars is an insignificant fraction of the total luminosity budget, but is observed to be correlated with the spin-down luminosity, and, as such, emission mechanisms explain this through the associated magnitude of the potential produced by unipolar induction of the rotating magnetic dipole (Chen & Ruderman, 1993).

Observationally, pulsars can be characterized in a variety of ways. One popular scheme is the so-called "P vs. $\dot{P}$" diagram which serves as an analog to the color-magnitude diagrams famously employed in stellar astrophysics. The most current version of this diagram is included as Figure 1.1 based on data from the Australia Telescope National Facility (ATNF) catalog (Manchester et al., 2005).

In Figure 1.1, The dominant cloud of "normal" pulsars is some 87% of the pulsars in the catalog. This population of pulsars has a median rotation period of $P = 0.58$ s and a median period derivative of $\dot{P} = 2.3 \times 10^{-15}$ while their median characteristic age $\tau_c = 4.7 \times 10^6$ yr, median surface dipole magnetic field $B_S \approx 1.2 \times 10^{12}$ G, and median spin-down luminosity $\dot{E} \approx 2.9 \times 10^{32}$ erg s^{-1}. Over the course of their lifetimes, isolated pulsars will spin down into the pulsar graveyard with a critical threshold occurring around $\dot{E}_{\mathrm{crit}} \approx 1.1 \times 10^{30}$ erg s^{-1} at the point where the field potential drops below a critical value thereby preventing the formation of electron-positron pairs above the polar cap (Chen & Ruderman, 1993). This canonical threshold termed

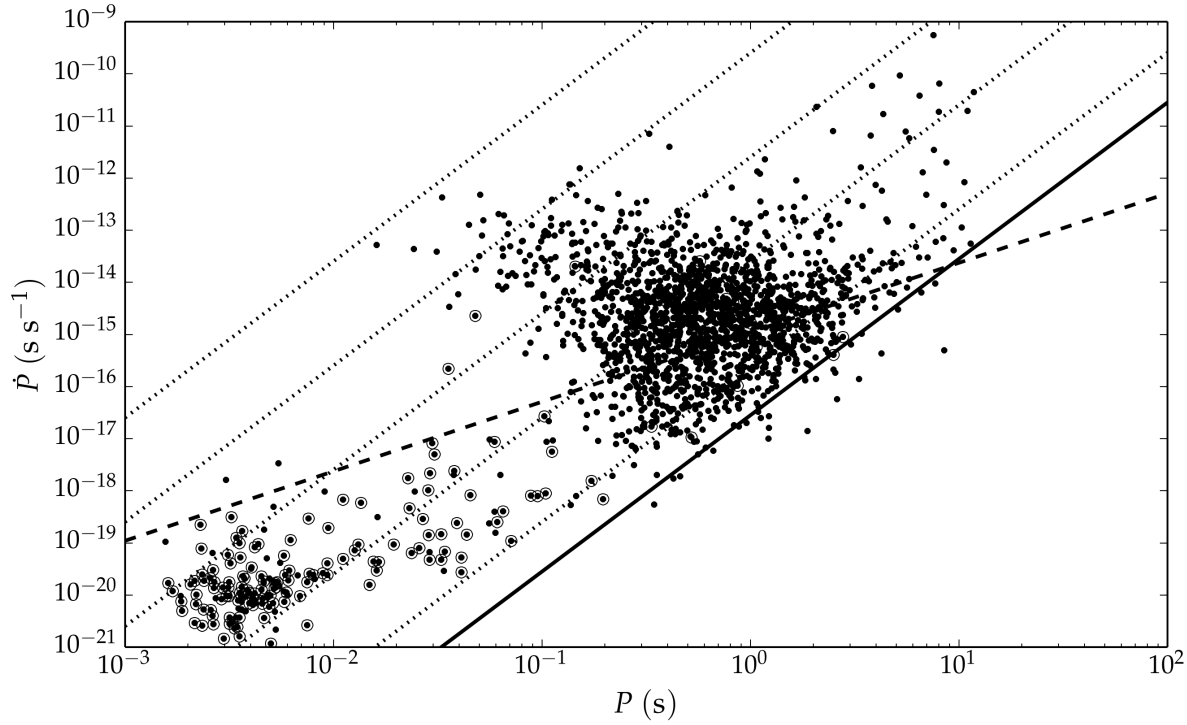

Figure 1.1: Period Derivative Versus Period of ATNF Catalog Pulsars.
All pulsars from the ATNF Catalog with known periods and period derivatives (Manchester et al., 2005). Known binaries are circled. The death line of Chen & Ruderman (1993) is the solid line, below which is the so-called "pulsar graveyard", while the maximum spin-up line of Bhattacharya & van den Heuvel (1991) given typical pulsar magnetic dipoles is the dashed line. Dotted lines are lines of constant $\dot{E}$ according to Equation 1.3. In order from lower right to upper left they are $\dot{E} = \{10^{31}, 10^{33}, 10^{35}, 10^{37}, 10^{39}\}$ erg s^{-1}. Note that the death line is closely coincident with $\dot{E} = 10^{30}$ erg s^{-1}.

the "death line" is plotted on the "P vs. $\dot{P}$" diagram in Figure 1.1 as the solid black line and the noticeable lack (but not complete absence) of pulsars beneath this line is evidence that, to first order, this mechanism prevents us from seeing lower $\dot{E}$ pulsars.

Pulsars that remain in binaries after initial formation can be spun up by means of accretion via an evolutionary scenario first proposed in 1982 independently by

Alpar et al. (1982) and Radhakrishnan & Srinivasan (1982) which proceeds roughly as follows: Binary pulsars enter into a stage of mass accretion where material from the secondary accretes onto the primary carrying with it angular momentum transferred to the neutron star, "spinning up" the object to higher rates than even the birth period. As this occurs, sources that have fallen to the right of the death line move to the left on the "P vs. $\dot{P}$" diagram. Though they have smaller magnetic fields than the main cloud of radio-detected pulsars, the recycled pulsars become detectable as radio sources again as the magnetic dipole radiation increases owing to the increased acceleration, provided accretion that causes plasma quenching of the radio signal stops. The end of accretion accompanies a disruption or complete removal of the companion from the system as must be the case in observed isolated millisecond pulsars. Since spin-up occurs in these systems, ages for millisecond pulsars derived from the typical assumptions of a constant spin down are not reliable (Kiziltan & Thorsett, 2010). Accreting pulsars can spin-up to maximum spin periods given by the period at the Alfvén radius, characteristic values for which assuming a magnetic dipole are plotted in Figure 1.1 as the dashed line (Bhattacharya & van den Heuvel, 1991).

This population of "millisecond pulsars" roughly sandwiched between the spin-up and death lines are are characterized by a median rotation period of $P = 4.2$ ms and a median period derivative of $\dot{P} = 1.8 \times 10^{-20}$ implying a median surface dipole magnetic field of $B_S \approx 2.8 \times 10^8$ G. Additionally, in keeping with proposed formation scenarios, the observed binary fraction of millisecond pulsars at $f_{\rm bin} \sim 60\%$ is significantly higher than the binary fraction of slower spinning pulsars of $f_{\rm bin} \sim 2\%$. Millisecond pulsars have median spin-down luminosities that are marginally higher than the normal population at $\dot{E} \approx 5.8 \times 10^{33}$ erg s^{-1} and since pulsar gamma-ray emission mechanisms are strongly correlated with spin-down luminosities, this implies that millisecond pulsars should be detectable as gamma-ray sources. Relevant histograms of the period, period derivative, surface magnetic field strength, and spin-

down luminosities for the entire ANTF catalog divided into the two subpopulations are presented in Figure 1.2 to further illustrate these defining characteristics.

1.1 Black Widow Pulsar(s): A Short History

Fruchter et al. (1988b) reported the discovery of a millisecond pulsar, PSR B1957+20 with a period of 1.6 ms and sinusoidal period modulation over the course of 9.17 hours. The object was distinctive as being the first eclipsing radio pulsar to be identified, with a radio signal gap of 44 minutes symmetric about the binary orbital phase of $\phi = 0.25$ (where the pulsar's ascending node corresponds to $\phi = 0$). As the pulsar mass function derived from this scenario implied a low mass for the companion of $M \sim 0.03\ M_{\odot}$, it was suggested that this object was likely an intermediate class of objects between Low-Mass X-ray Binaries (LMXBs) and isolated millisecond pulsars (Ruderman et al., 1989a). The radio eclipses are consistent with a high plasma-density environment when the line-of-sight to the pulsar is occulted by the environment surrounding the companion, and this feature was cited as evidence that the companion was being ablated by action from either high-energy radiation from the pulsar or by the pulsar's particle wind (Ruderman et al., 1989b). The pulsar came to be known as the "Black Widow Pulsar" because of the ongoing ablation of its companion and it now serves as the prototype for an entire class of binary millisecond pulsars in tight orbits ($P_{\rm orb} \leq$ 1 d) with low-mass ($M_{\rm c} \leq 1\ M_{\odot}$) companions.

The eclipses seen in B1957+20 are attributed to attenuation of the radio signal as it passes through a dense plasma. To cause such an environment and to accommodate the prediction that isolated millisecond pulsars are the end result of such "black widow" systems, the models proposed to include a $\dot{M} > 10^{15}$ g s^{-1} outflow from the companion object produced by heating through irradiation of the companion either by high-energy photons from the neutron star itself or by secondary emission from

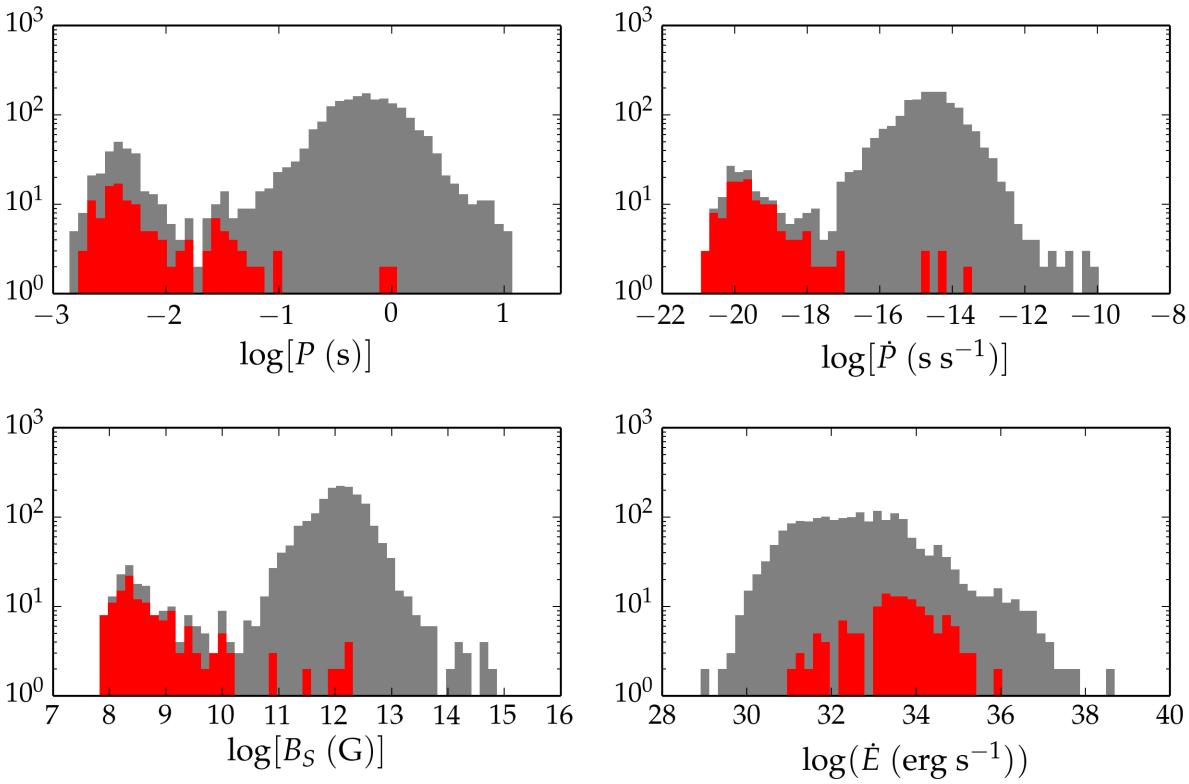

Figure 1.2: Four Histograms Illustrating the Characteristics of Pulsars from the ATNF Catalog.

The histograms are scaled logarithmically to emphasize the division between the millisecond and young pulsar populations with the histograms for binary pulsars shown in red and the histogram for the entire catalog in grey. The top left plot shows the distribution of pulsar periods emphasizing that most binaries are millisecond pulsars. The remaining histograms are as follows: top right) measured period derivatives, bottom left) surface magnetic fields as given by equation 1.2, bottom right) spin-down luminosity as given by Equation 1.3.

the stand-off shock between the pulsar wind and the companion (Kluzniak et al., 1988; Phinney et al., 1988). However, a high flux-density in radio observations at 20 cm wavelength during the eclipses implies a plasma environment with a density of approximately $n \sim 10^9$ cm^{-3}, and led authors to contend that the secondary should be close to filling its Roche lobe in order to allow for mass loss through something

like an excretion disk (Fruchter & Goss, 1992). To achieve this, as well to account for optical observations and period variations, Applegate & Shaham (1994) proposed that the observed luminosity of the secondary could be strongly influenced by a tidal heating mechanism. Further theoretical investigations by King et al. (2003) into the abundance of such systems in globular clusters compared to the field proposed that complete ablation of the companion was not necessary to explain the incidence of isolated millisecond pulsars and that, rather, close encounters could be a major channel for the production of millisecond pulsars as well as means by which isolated millisecond pulsars could be produced and ejected from globular clusters into the field.

An optical detection of the B1957+20 system was made soon after its discovery (Kulkarni et al., 1988), and light curves were characterized thereafter by van Paradijs et al. (1988) and Fruchter et al. (1988a). The modulation of the flux coming from the secondary is phase-matched so that the object is observed to be brightest in all bands at $\phi = 0.75$ and dimmest at $\phi = 0.25$. Irradiation from the pulsar heats the side of the secondary tidally locked to face the pulsar, and this heating drives the wind off the secondary that increases the local plasma density near the companion required to explain the radio eclipses. For any orbit different from a face-on inclination, this orbital geometry predicts the hot side of the companion preferentially facing the line of sight at phase $\phi = 0.75$ while the cold side is most visible at phase $\phi = 0.25$. In B1957+20, a significant fraction, up to $f = 0.01$, of the directed energy flux from the pulsar to the secondary is reprocessed as heating, changing the secondary's emitted bolometric intensity by a factor of ~ 70. While the observed heating can explain the plasma density necessary for the eclipse, it is still an outstanding question as to whether the mass loss rate is high enough to allow for complete ablation and thus serve as the direct link between LMXBs and isolated millisecond pulsars (Levinson & Eichler, 1991). Additionally, a relatively large rotational luminosity ($\dot{E}_R \sim \dot{P}P^{-3}$ implies that millisecond pulsars can have significant relativistic winds which led ob-

servers to search for an associated pulsar wind nebula. The interaction of winds of the black widow pulsar with the interstellar medium have been seen both in X-ray emission (Stappers et al., 2003) and associated with Hα emission from a stand-off bow shock (Kulkarni & Hester, 1988).

Binary millisecond pulsar systems are found in abundance in globular clusters including 23 found in a single globular cluster 47 Tucanae (Camilo & Rasio, 2005). Stappers et al. (1996b) discovered the second black widow pulsar J2051–0827 in the field with a rotational period of 4.5 ms and an orbital period of 2.38 hrs. The irradiated companion was detected with a phase-matched light-curve mimicking the original black widow pulsar and lending further support to the model of irradiation of the companion (Stappers et al., 1996a). The Parkes High-Latitude pulsar survey identified an additional black widow pulsar candidate J0610–2100 with a rotational period of 3.86 ms and a 6.86 hr orbital period, though neither a radio eclipse nor an optical candidate has been detected for this object yet (Burgay et al., 2006).

Another intriguing object, detected in the radio as FIRST J1023+0038 was first improperly identified as a candidate cataclysmic variable by Bond et al. (2002), but the companion light curve was later found to be smoothly varying by Woudt et al. (2004) similar to the heating + ellipsoidal curves of B1957+20. Thorstensen & Armstrong (2005) went on to propose that the companion could be a neutron star and that the system might be changing on a timescale of years from an accreting system to one that had no accretion disk. This hypothesis was later confirmed by the 1.69 ms radio pulsar discovery of PSR J1023+0038 by Archibald et al. (2009) who also reported no evidence of a disk in the system at the time of their observations seven years off from the initial detection. Parallax distances using the Very Long Baseline Array combined with optical observations to obtain the result that the neutron star has a mass $M_{\rm NS} = 1.71 \pm 0.16 M_{\odot}$ (Deller et al., 2012), while Patruno et al. (2014) reports that as of late 2013 the accretion disk has returned.

One of the main motivations for studying such systems comes from the ongoing challenge in astrophysics to discover the highest-mass neutron star. Finding that object will directly constrain the equation of state of ultra dense matter – something that cannot be achieved in terrestrial laboratories – since different models predict different highest possible neutron-star masses. Indeed, the highest neutron star masses measured to date have already ruled out certain models (Steiner et al., 2013) and there are no modern models which permit masses in excess of $M_{\rm NS} > 2.9 M_{\odot}$ (Chamel et al., 2013). The most massive neutron stars are likely to be millisecond pulsars due to their accretion history, and millisecond pulsars in binaries are the ones where masses can be measured directly. These short period binaries exhibit two observable forms of orbital variation in the optical and infrared bands: 1) an irradiated light curve associated with heating of the side of the companion facing the neutron star (often in excess of $10,000$ K), and 2) ellipsoidal variations due to the companions being relatively close to filling their Roche lobes. These optical/infrared signals modulate in phase with the system parameter fit from radio data (e.g., Reynolds et al., 2007) and can be used to constrain other system parameters, most importantly neutron star masses. Indeed, it was only after high-quality photometric light curves were obtained for the prototypical system, PSR B1957+20, constraining the inclination angle, Roche lobe filling factor, and temperature profile of the secondary (Reynolds et al., 2007), that van Kerkwijk et al. (2011) were able to constrain the mass of the neutron star to $M_{\rm NS} > 1.9\ M_{\odot}$ by also using the radial velocity curve from spectroscopy.

1.2 Gamma-ray Astronomy of Millisecond Pulsars

Gamma-ray astronomy as a subject began with theoretical plausibility work done in the 1940s and 1950s that invoked a variety of possible engines including cosmic-ray collisions (Feenberg & Primakoff, 1948), supernovae (Hayakawa, 1958), inverse Compton-scattering in shocks and other energetic environments (Felten & Morrison,

1963), and both synchrotron emission and curvature radiation seen in locations with large magnetic field densities (Felten & Morrison, 1966). Most gamma-ray sources can be well-matched by emission mechanisms of the final two varieties, though, in the case of synchrotron radiation, there is a fairly robust upper-limit on the energy of photons generated by electrons of approximately $E_{\max} \sim 70$ MeV (Muñoz-Darias et al., 2009) which means that typical emission mechanisms above this limit are due to inverse Compton scattering of photons off of energetic electrons and, in the case of high magnetic fields as what is present in pulsars, curvature radiation.

The first cosmic gamma-rays were detected by Kraushaar et al. (1965) using the Explorer XI experiment and presented weak evidence of gamma-rays emanating from the galactic plane, though the results were also consistent with an isotropic background. Later observations with the Small Astronomy Satellite (SAS)-2 (Fichtel et al., 1975) and COS-B (Swanenburg et al., 1981) confirmed the existence of gamma-ray point-sources which were associated with the Crab and Vela pulsars and what came to be known as blazars (Angel & Stockman, 1980). The *Compton Gamma-Ray Observatory*'s Energetic Gamma Ray Experiment Telescope (EGRET) provided the first all-sky map of the gamma-ray sky and catalogued 270 persistent sources – enough to make source identification in gamma-ray astronomy into an industry (Fierro et al., 1995).

Gamma-ray astronomy received an incredibly potent shot in the arm with the 2008 launch of the *Fermi Gamma-ray Space Telescope* (Meyers, 2014). Of particular interest to this work is the observatory's primary instrument, the Large Area Telescope (*Fermi*/LAT, hereafter LAT), a pair-conversion calorimeter array sensitive to gamma rays ranging in energy from 20 MeV to in excess of 150 GeV with a point-source localization capability of 0.3–2 arcmin (Fermi-LAT Collaboration, 2009b). The first LAT source catalog was released in preliminary form in January 2010 with 1451 4σ sources detected and characterized in the 100 MeV to 100 GeV range identified over a mission integration time of 11 months, including 690 unassociated sources (Abdo

et al., 2010). Two years later, the second source catalog was released based on the first 24 months of LAT data which increased the number of sources to 1873 while only 575 were at the time of publication still considered to be unassociated with a known counterpart. The third source catalog is still in preparation (Thompson et al., 2014).

Millisecond pulsars, the primary subject of this work, were predicted to be sources of gamma rays by Usov (1983) and Chen (1991). Gamma rays are produced by millisecond pulsars because their energy loss due to dipole radiation is similar to young pulsars while their magnetic fields at the surface are smaller than those in young pulsars (see Figure 1.2), and higher energy photons are more likely to escape lower magnetic field environments (Srinivasan, 1990). Unfortunately, the search for pulsed gamma-ray detections of millisecond pulsars had been essentially unsuccessful during the first- and second-generation gamma-ray observatories (Fierro et al., 1995). Even though EGRET discovered 270 sources, its point spread function had a full-width half-maximum of 6° at 100 MeV which only allowed for the confirmed identification of six ordinary gamma-ray pulsars (Hartman et al., 1999) and a single marginal 3.5σ detection of the millisecond pulsar J0218+4232 by Kuiper et al. (2000). However, millisecond pulsars do contribute to the gamma-ray background as well as to the globular cluster gamma-ray flux seen by EGRET and possibly COS-B (Bhattacharya & Srinivasan, 1991; Sturner & Dermer, 1994). Even with a lack of sources prior to the launch of *Fermi*, the predictions were that many millisecond pulsars would be identified as sources by LAT (Story et al., 2007; Zhang et al., 2007). This prediction has proven to be correct; approximately one quarter of the pulsars positively identified by the LAT are millisecond pulsars (Fermi-LAT Collaboration, 2009a; The Fermi-LAT Collaboration, 2011).

Fermi's ongoing mission coincides with campaigns to discover millisecond pulsars by teams at various radio telescopes around the world including Parkes (Weltevrede et al., 2010), Effelsberg (Barr et al., 2013), Nançay (Cognard et al., 2011), and Green

Bank (Lynch & Bank North Celestial Cap Survey Collaborations, 2013). While blind surveys suffer from the computational difficulties associated with searching through tremendous amounts of parameter space, the Fermi source catalog provides a convenient localization capability for unidentified sources to within arcminutes. Approximately 40 rotation-powered binary millisecond pulsars with orbits $P_{\rm orb} < 1$ d have been identified by these consortia (Ray et al., 2012) and many of these systems exhibit radio eclipse features around the orbital phase $\phi = 0.25$. As the population of radio-eclipsing binary millisecond pulsars has burgeoned, a bifurcation in the population has been identified that is yielding rich new phenomenology for these systems. In addition to the typical "black widows" similar to B1957+20, which, as a class, have mass functions at about $f \sim 10^{-5} M_\odot$, a new subpopulation of so-called "redbacks" with binary mass functions in excess of $f \geq 10^{-3} M_\odot$ are lately of considerable interest (Roberts, 2011). The radio eclipse properties of these redback systems are qualitatively much different than those of canonical black widow pulsars; they exhibit longer eclipses that are more irregular and variable in their phase of onset and duration (Ransom, personal communication). Extrapolating the distinction between the subpopulations to plausible masses for the millisecond pulsars ($M_{\rm NS} \sim 1.4 M_\odot$) implies that redback companions are of main sequence or subdwarf masses ($M_{\rm c} \gtrsim 0.2 M_\odot$) while the black widow companions are the masses of brown dwarfs or stripped white dwarf cores similar to those seen in ultracompact LMXBs (Rappaport et al., 1982; Deloye & Bildsten, 2003). Short-period millisecond pulsars with redback-sized masses include PSR J1023+0038, while another example of a transitioning pulsar, IGR J18245–2452, was recently identified in the globular cluster M28 as switching from being a rotation powered to being an accretion powered pulsar (Papitto et al., 2013), both characterized as "missing link" pulsars for this reason. Indeed, many redbacks seem to be in transition between LMXBs and rotation-powered pulsars.

Since the launch of *Fermi*, optical follow-up campaigns intent on discovering and characterizing the comparisons of short-period binary millisecond pulsar systems have

yielded results aplenty. Romani et al. (2012) obtained a lower mass limit from model fits for a *Fermi*-detected system, PSR J1311–3430, of $M_{\rm NS} > 2.1\ M_\odot$. These measurements are consistent with the highest dynamical measurement of a neutron star to date of $1.97 \pm 0.04\ M_\odot$ for J1624–2230 (Demorest et al., 2010). The field continues to be very active. Recently, Kaplan et al. (2013) used a radial velocity measurements of the optical companion of J1816+4510 to obtain an inclination-angle dependent neutron star mass of $M_{\rm NS} \sin^3 i = 1.84 \pm 0.11\ M_\odot$. Similarly Crawford et al. (2013) detected the companion to the redback J1723–2837 and used spectroscopic follow-up to obtain an inclination-angle dependent neutron star mass of $M_{\rm NS} \sin^3 i = 0.3 \pm 0.1 M_\odot$ from which they predict an inclination angle for the system of $i \leq 41^\circ$.

This work continues with an investigation of certain binary millisecond pulsars first detected in the LAT source catalog and then confirmed through radio follow-up. The primary results of this have been submitted to the Astrophysical Journal in Schroeder & Halpern (2014), and the following chapters will borrow heavily from that work. I will proceed in Chapter 2 to outline the means by which target selection occurred for the fields that my advisor, Professor Jules Halpern, and I observed over the course of my thesis work. Subsequent chapters will deal with data reduction, data analysis, and modeling, with the main results summarized in Section 5.2.

Chapter 2

Target Selection

The Second *Fermi* LAT Source Catalog (The Fermi-LAT collaboration, 2013) identifies point-like and extended gamma-ray sources and further attempts to associate each source with a counterpart. An all-sky distribution of these sources is shown in Galactic coordinates in Figure 2.1. The associations of LAT sources with pulsar counterparts is done mostly with radio follow-up, though there are ways of identifying pulsars independent of this method. In particular, the pulsar gamma-ray spectra in the *Fermi* range deviate significantly from power-laws. This can be theoretically understood by considering the production of gamma rays by curvature radiation that has characteristic frequencies $\nu_c \sim \gamma^3 c/r_c$ where γ is the Lorentz factor and r_c is the radius of curvature of the field lines along which the particles are accelerated. The associated spectrum is predicted to follow an exponential cut-off after the peak energy, $E \sim h\nu_c$, similar to synchrotron radiation (The Fermi-LAT Collaboration, 2010). The extent to which the spectrum fits such a curved model compared to a simple power-law fit is characterized by a curvature significance statistic reported in the catalog. Additionally, unlike blazars, pulsars rarely exhibit variability and generally are below the threshold variability index value for the *Fermi* catalog of > 41.6, which is the $> 99\%$ confidence interval for source variability. Thus, the best targets for

finding pulsars are those sources which have small variability index and large curvature significance. Figure 2.2 shows a plot that cleanly discriminates between the two populations based on *Fermi* catalog data, and it is on this basis in part that certain previously unassociated sources were judged to be viable targets for radio follow-up, and, in at least one instance, a "black widow-type" pulsar system was discovered by recognizing an irradiated light curve in a blind optical search of an appropriate unassociated source (Kong et al., 2012). The relevant data from the *Fermi* catalog for the fields we observed is tabulated in Table 2.1.

Since millisecond pulsars are strong gamma-ray sources, the technique of searching for radio-loud pulsars in the error box of an unassociated gamma-ray source discovered by the *Fermi* LAT has been fruitful. As of this writing, the *Fermi* team has identified gamma-ray sources associated with 51 millisecond pulsars, all but one of these associated with radio counterparts and 39 have been determined to be in binary systems (The Fermi-LAT collaboration, 2013).

Radio observations of binary millisecond pulsars allow for the identification of eclipse features, while ephemeris fits precisely determine certain system parameters including the position on the sky, binary period ($P_{\rm orb}$), epoch of the ascending node (T_0), and projected semi-major axis (x) (Ray et al., 2012). These values can be related to the physical characteristics of the systems through the binary mass function

$$f = \frac{4\pi^2 x^3}{G P_{\rm orb}^2} = \frac{(M_{\rm c} \sin i)^3}{(M_{\rm NS} + M_{\rm c})^2} \tag{2.1}$$

where $M_{\rm NS}$ is the mass of the neutron star, $M_{\rm c}$ is the mass of the companion, and i is the inclination angle of the orbit. The determination of masses for the objects in the system requires measuring the inclination angle and one of the object masses or the mass ratio ($Q \equiv M_{\rm NS}/M_{\rm c}$) (Lorimer & Kramer, 2004).

Ray et al. (2012) provides the *Fermi* LAT team's list of radio-identified binary millisecond pulsars for which various radio-measured properties have been obtained in-

cluding the pulsar spin periods, binary mass functions, orbital periods, and dispersion measures. Of particular interest for optical follow-up campaigns is the positional accuracy to the sub-arcsecond level determined from the radio ephemerides which is a great improvement over the ten arcminute-scale error boxes associated with the LAT confidence regions. After detecting the companion object, it is possible to constrain the inclination angle and the blackbody temperature profile of the secondary through photometry alone. An example of such a study is one done by Breton et al. (2013) who identified the optical counterparts of four Fermi-detected binary millisecond pulsars and measured the magnitudes in various filters at a number of phases over each orbit. It has generally been assumed that meaningful constraints on masses would require radial velocity data, but photometrically stable and relatively high signal-to-noise light curves can give model constraints on the masses of the primary and secondary, especially if ellipsoidal variations are detected. Using photometry alone to obtain mass constraints was first suggested in Avni & Bahcall (1975) and a similar technique was used by Jackson & Carlberg (2012) to constrain the mass of exoplanets.

In this work, I report on observations made over the course of seven runs at MDM Observatory of eight fields containing binary millisecond pulsars with periods less than one day. Of the eight systems, we detect optical counterparts of four, three of which have been reported in the literature and one of which is a novel detection. Two of these four were bright enough to allow us to obtain phase-resolved optical light curves in BVR filters while detection upper limits were made for the others. In the next chapter, I describe the observations and the data reduction procedures including the positive identifications and upper limits of optical counterpart detections. Chapter 4 makes use of the ELC code (Orosz & Hauschildt, 2000) modeling to do parameter fitting for two of the best-observed objects, and, in the final chapter, Section 5.1 includes a discussion of possible interpretations and implications of our results.

Table 2.1: Table of relevant data from the Second *Fermi* Source Catalog (The Fermi-LAT Collaboration, 2011) of the eight fields observed in this work. After the catalog's finalization, Kaplan et al. (2012) positively identified PSR J1816+4510 as being associated with 2FGL J1816.5+4511. The Power Law Index is the best-fit model for an exponentially cut-off power law while the Spectral Index is best fit and uncertainty ignoring any curvature of the spectrum. Flux Density is measured at the reported Pivot Energy which corresponds roughly to the location of the break in the power-law (specifically defined as the decorrelation energy for the power-law fit to each spectra where the error in the differential photon flux is minimal).

Pulsar	J0023+0923	J1745+1017	J1810+1744	1816+4510
$l(^\circ)$	111.504	34.844	44.6179	72.8544
$b(^\circ)$	-52.8456	19.2289	16.7586	24.7412
Significance	8.3	8.6	18.3	13.0
Flux Density	1.4×10^{-12}	1.8×10^{-12}	1.9×10^{-11}	1.1×10^{-12}
(photons cm^{-2} MeV^{-1} s^{-1})	$\pm 2 \times 10^{-13}$	$\pm 2 \times 10^{-13}$	$\pm 2 \times 10^{-12}$	$\pm 1 \times 10^{-13}$
Pivot Energy (MeV)	903.307	973.723	529.049	1146.1
Spectral Index	2.3 ± 0.1	2.3 ± 0.1	2.2 ± 0.1	2.1 ± 0.1
Curvature Significance	3.32	2.49	4.47	2.77
Power Law Index	2.26	2.34	2.41	2.11
Variability Index	25.17	22.26	17.84	22.05
Pulsar	J2047+1053	J2214+3000	J2215+5135	J2234+0944
$l(^\circ)$	57.0204	86.8786	99.8915	76.2872
$b(^\circ)$	-19.57	-21.6789	-4.18332	-40.4287
Significance	6.2	34.7	11.0	9.7
Flux Density	6.5×10^{-13}	7.6×10^{-12}	8.7×10^{-12}	1.2×10^{-12}
(photons cm^{-2} MeV^{-1} s^{-1})	$\pm 1.2 \times 10^{-13}$	$\pm 4 \times 10^{-13}$	$\pm 1 \times 10^{-13}$	$\pm 2 \times 10^{-13}$
Pivot Energy (MeV)	1211.93	914.921	1642.68	1049.0
Spectral Index	2.3 ± 0.1	1.1 ± 0.1	1.9 ± 0.2	2.2 ± 0.1
Curvature Significance	2.95	7.19	4.06	3.58
Power Law Index	2.26	2.00	2.04	2.23
Variability Index	26.58	22.77	31.16	37.87

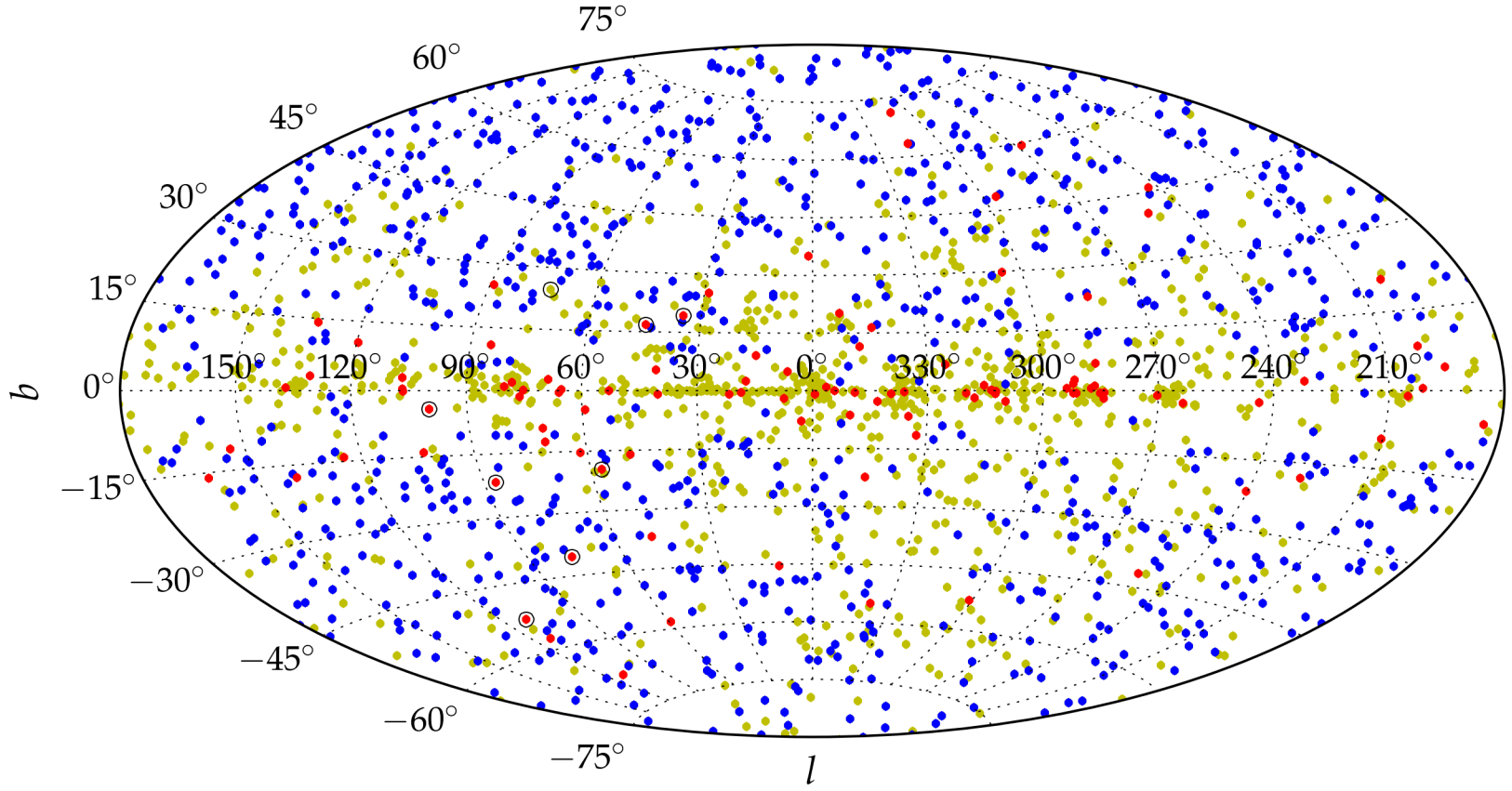

Figure 2.1: Source Locations from the Second *Fermi* Source Catalog.
Aitoff projection in galactic coordinates of the sources from The Fermi-LAT collaboration (2013). In blue are blazars, active galactic nuclei, radio galaxies, and Seyfert galaxies. In red are pulsars. All other sources (the majority of which are unassociated) are in yellow. The eight sources observed in this work are circled in black. Note that PSR J1816+4510 was not yet associated with the field in which it is found at the time of catalog production thus it is the sole yellow point that is circled.

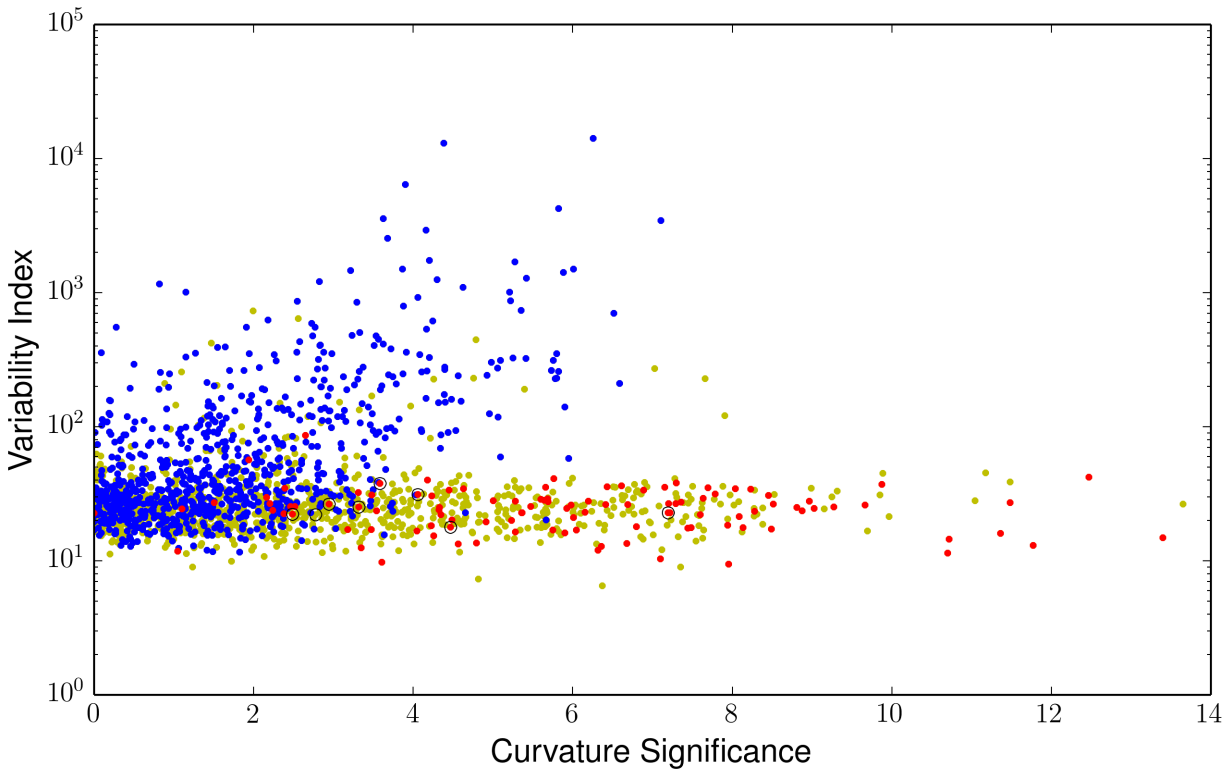

Figure 2.2: Curvature Significance vs. Variability Index
Plot of Curvature Significance versus Variability Index of the sources from The Fermi-LAT collaboration (2013). Color scheme follows Figure 2.1, with the eight sources observed in this work again circled in black. A Variability Index > 41.6 is the $> 99\%$ confidence interval for a variable source.

Chapter 3

Observations and Data Reduction

Over the course of eight observing runs at MDM observatory from May 2010 to August 2011, my advisor, Prof. Jules Halpern, and I observed the positions of various *Fermi*-detected and radio-confirmed binary millisecond pulsars using the 1.3 meter McGraw-Hill and the 2.4 meter Hiltner telescopes. For the first six runs, we employed one of either two thinned backside illuminated (a 2048×2048 pixel CCD called "Echelle" and a 1024×1024 pixel CCD called "Templeton") or, one thick frontside illuminated imaging CCD (a 2048×2048 pixel CCD called "Nellie") with Harris B, V, and R filters. The MDM CCD-control software failed for our last two runs in August 2011, so we instead used newly commissioned OSMOS and Red4K LBNL 250 micron thick, fully depleted p-channel 4096×4096 pixel CCDs built by Ohio State University Astronomy Department. The goal was to detect the optical counterparts to binary millisecond pulsars and, when possible, obtain full phase-resolved light curves in each of the three filters.

The eight fields observed are all listed in Table 2.1 and their associated pulsars are discussed in Ray et al. (2012) with ephemerides for each provided to us by the radio follow-up team. Table 3.1 notes the observations made of each along with their measured magnitudes in various filters or upper limits. Previously, three of these

systems have been detected by Breton et al. (2013), J0023+0923, J1810+1744, and J2215+5135. According to their observations, only J2215+5135 and J1810+1017 are bright enough for our campaign to have been able to detect a signal, and these are, in fact, the two objects for which we obtained complete phase-resolved coverage. Additionally, J1816+4510 was identified by Kaplan et al. (2013) as being bright enough to be identified in the Digitized Sky Survey, and we confirm detection of this source. In all, we detect four counterparts: J1810+1744, J1816+4510, J2214+3000, and J2215+5135, one of which, J2214+3000 is a novel detection. The relevant details of the observations of the eight fields observed is summarized in Table 3.1 and discussion of the objects proceeds in the following two subsections.

Conditions over the observing runs often varied with intermittent cloud cover occurring on some nights and considerable particulate matter observed in the atmosphere on the observing run of MJD 55798 to 55803. In instances of non-photometric conditions, the data were only used for differential photometry rather than absolute photometric calibration. Additional electronic noise and interference patterns affected observations on MJD 55452 as well as the entire run that used the Red4K CCDs with the latter issue being so prohibitive as to make standard reduction schema, in particular flatfielding, impossible. In both of those cases, differential photometry was only attempted if calibration of the images indicated minimal systematic uncertainties (that is, if the background counts were relatively constant in the area of interest).

The images were reduced using the `ccdproc` IRAF routine for bias subtraction and flatfielding while, if necessary, astrometric solutions were obtained using `imcoords`. If needed, as in the case of obtaining upper limits, images taken with the same instrument in an observing run were combined using the `imalign` and `imcombine` routines. Aperture photometry was done using the `apphot` package for a range of apertures with absolute photometric calibration done using large apertures and differential photometry done using small apertures (the precise sizes chosen on the basis

of the minimum of the photometric errors in the case of small apertures and in consideration of field crowdedness in the case of large apertures). Absolute photometry was calibrated using interspersed observations of Landolt standard fields (Landolt, 1992) which were used to confirm both the photometric offsets, variation with airmass, and any color-correction terms. For J1810+1744 and J2215+5135, secondary standards for differential photometry were chosen on the basis of observed photometric stability. For both objects, we measured the zero-point calibration to be precise to within bootstrap errors of 0.1 mag.

Phase-resolution was done using published ephemerides where possible and some provided by means of private communication. The orbital phase of each observation was computed by applying a heliocentric correction to the observation time ($t_{\rm obs}$), subtracting the result from $\phi = 0$ time as measured from the radio ephemeris (T_0) for each observation and finding the fractional remainder of the orbit. Thus

$$\phi = \frac{(t_{\rm obs} - T_0) \bmod P_{\rm orb}}{P_{\rm orb}} \tag{3.1}$$

is used where, by convention, $\phi = 0$ is the phase of the epoch of the ascending node. The expected optical signal should exhibit a maximum due to irradiation at $\phi = 0.75$ while the minimum associated with the line-of-sight visibility of the nonirradiated side occurs at $\phi = 0.25$. The normally smaller ellipsoidal variations exhibit peak brightness at $\phi = 0$ and $\phi = 0.5$ respectively.

In the case of J1810+1744, Breton et al. (2013) report that a neighboring star is a possible contaminant near minimum. My attempts to detect these faint contaminant stars by combining images near minimum and performing PSF-fitting were unsuccessful in the sense that there was no additional flux or extended emission detected to within the errors of the PSF-fit, and so I concluded that aperture photometry was likely to be accurate enough for the differential photometry analysis.

Below I discuss the findings for each object individually together with related results

from previous work.

3.1 J2214+3000

J2214+3000 was identified by Ransom et al. (2011) and the radio data therein provided indicates a rotational period of the pulsar of 3.1 ms, a binary orbital period of 9.8 hrs, and a binary mass function $f = 8.7 \times 10^{-7} M_{\odot}$. Of particular interest to this work is that the precise position of the source (epoch J2000) is given at $22^{\rm h}\ 14^{\rm m}\ 38\overset{\rm s}{.}8460(1)$ in right ascension and $+30^{\circ}\ 00'\ 38\overset{''}{.}234(4)$ in declination. To within astrometric errors, this is consistent with the coordinates where we detected the companion.

I combined R-band images at $\phi = 0.75 \pm 0.1$ to obtain the detection listed in Table 3.1 while the lower limits of R included combinations of images from all other phases. Additionally, combinations of the B images which range from $0.1 \leq \phi \leq 0.6$ yielded a null result. See Figure 3.1 for a comparison image.

The detection limits of the observing capabilities of the facilities at MDM observatory are such that we were unable to obtain a complete photometric light curve for J2214+3000. For our observing runs, we determined it was an unsuitable candidate for complete phase coverage and model-fitting in spite of its detection for three reasons: 1) its long orbital period makes obtaining full phase coverage in multiple filters prohibitive, 2) it is the faintest detection in our sample and characterization of its light curve outside of peak brightness near $\phi \sim 0.75$ would be unlikely, and 3) there is source confusion with a nearby bright $R = 14.1$ some $14''$ to the west, and the bright source's diffraction spike is oriented in exactly the same direction causing source confusion for our deepest observations which is why, for example, we can only report upper limits for minimum in Table 3.1 in spite of having a combined exposure time > 100 minutes within $\Delta\phi = 0.1$ of $\phi = 0.25$.

3.2 J1816+4510

J1816+4510 was first identified as an eclipsing binary millisecond pulsar by the 350 MHz Green Bank North Celestial Cap Survey with a pulsar rotational period of 3.2 ms, binary orbital period of 8.6 hrs, and binary mass function $f = 1.7 \times 10^{-3} M_{\odot}$. Although its mass function is consistent with redbacks, its optical counterpart was identified by Kaplan et al. (2012) as being a white dwarf with R = 18.3 and $T_{\rm eff}$ = 15 000 K with no evident phase-dependent heating, though typical effective irradiation luminosities measured in other short period binary systems would not be detectible with such an intrinsically hot companion. Our six observations made of this object are consistent with no variability to within measured uncertainties, so no constraints can be placed on system parameters. Determination of such will require a more-dedicated observational campaign similar to the ones we conducted on J1810+1744 or J2215+5135.

3.3 J1810+1744

J1810+1744 is a $P_{\rm rot} = 1.7$ ms pulsar discovered with the 350 MHz frequency channel at the Green Bank Telescope (GBT) (Hessels et al., 2011) with an orbital period of $P_b = 3.6$ hrs and binary mass function $f = 4.4 \times 10^{-5} M_{\odot}$. Our observations were able to isolate the optical signature of the secondary over the course of a number of runs, and complete phase coverage in three bands was obtained as reported in Table 3.1. At minimum, the source is near the detection limits, and for approximately half the observations taken between phases $0.15 \leq \phi \leq 0.35$ we are only able to reliably report upper limits. The measurements along with the uncertainties are plotted in Figure 4.1.

The measurements are somewhat in tension with the reported light curve fits of

Breton et al. (2013). Using the Lupton (2005) transformation equations, our R and V light curves and the i and g light curves from Breton et al. (2013) imply the same r-band light curve to within $|\Delta r| < 0.3$. However, our B light curve when matched to their g light curve gives a r-band light curve that differs at minimum by more than $|\Delta r| > 3$. I propose therefore that there is a much steeper drop in the blue-end of the spectrum for this object which would imply that their best-fit g light curve is too bright at minimum. To provide a level of corroboration, I note that a single faint $g = 22.8$ detection near minimum ($\phi = 0.2$) *is* consistent with our observations in the sense that if that measurement is taken to be the g magnitude at minimum and the transformation is redone at that phase, a prediction for an r-band magnitude that is within $|\Delta r| < 0.3$ of the initial prediction is found.

I report on how I obtained a set of best-fit model light curves on the basis of these observations in Section 4.1.

3.4 J2215+5135

J2215+5135 was also discovered with the 350 MHz GBT search with a $P_{\rm rot} = 2.6$ ms, $P_b = 4.1$ hrs, a binary mass function $f = 3.6 \times 10^{-3} M_\odot$, and observed radio eclipses. Full phase coverage was obtained as reported in Table 3.1 and the object's photometry is well-constrained at minimum. The measurements along with the uncertainties are plotted in Figure 4.2. As a redback, this object exhibits less orbital modulation than black widows consistent with a larger-mass companion.

Breton et al. (2013) fits four observations in the i-band to a light curve that, when transformed using the equations of Lupton (2005) to our R-band light curve, give a prediction of r at $\phi = 0.45$ consistent to within $|\Delta r| < 0.1$ of the prediction when transforming their observation of $g = 19.2$ to our observations of B, V, and R at the same phase.

I report on how we obtained our best-fit model light curves on the basis of these observations in Section 4.2.

3.5 J0023+0923

J0023+0923 was identified with the 350 MHz GBT search with a $P_{\rm rot} = 3.1$ ms, $P_b = 3.4$ hrs, a binary mass function $f = 2.4 \times 10^{-6} M_\odot$ but with no observed radio eclipses. The optical counterpart was detected by Breton et al. (2013) with a brightness at maximum of $i = 21.7$ according to their best-fit model. We report null results in B, V, and R-bands in Table 3.1.

3.6 J1745+1017

J1745+1017 was discovered with the Effelsberg Radio Telescope using the 1.32 GHz channel and has $P_{\rm rot} = 2.7$ ms, $P_b = 17.5$ hrs, a binary mass function $f = 1.4{\times}10^{-6} M_\odot$ (Barr et al., 2013). Performing a photometric analysis at the reported position of $17^{\rm h}$ 45m $33\overset{\rm s}{.}8371(7)$ $+10^\circ$ $17'$ $52\overset{''}{.}523(2)$ of images combined within a few hours of $\phi = 0.75$ yielded the null result as reported in Table 3.1.

3.7 J2047+1053

According to Ray et al. (2012), J2047+1053 was discovered at the Nançay Radio Telescope and has $P_{\rm rot} = 4.3$ ms, $P_b = 2.9$ hrs, a binary mass function $f = 2.3 \times 10^{-5} M_\odot$. I report null results in B, V, and R-bands in Table 3.1.

3.8 J2234+0944

According to Ray et al. (2012), J2234+0944 was discovered using the Parkes Radio Telescope and has $P_{\rm rot} = 3.6$ ms, $P_b = 10$ hrs, a binary mass function $f = 1.7 \times 10^{-6} M_\odot$. I report null results in the R-band in Table 3.1.

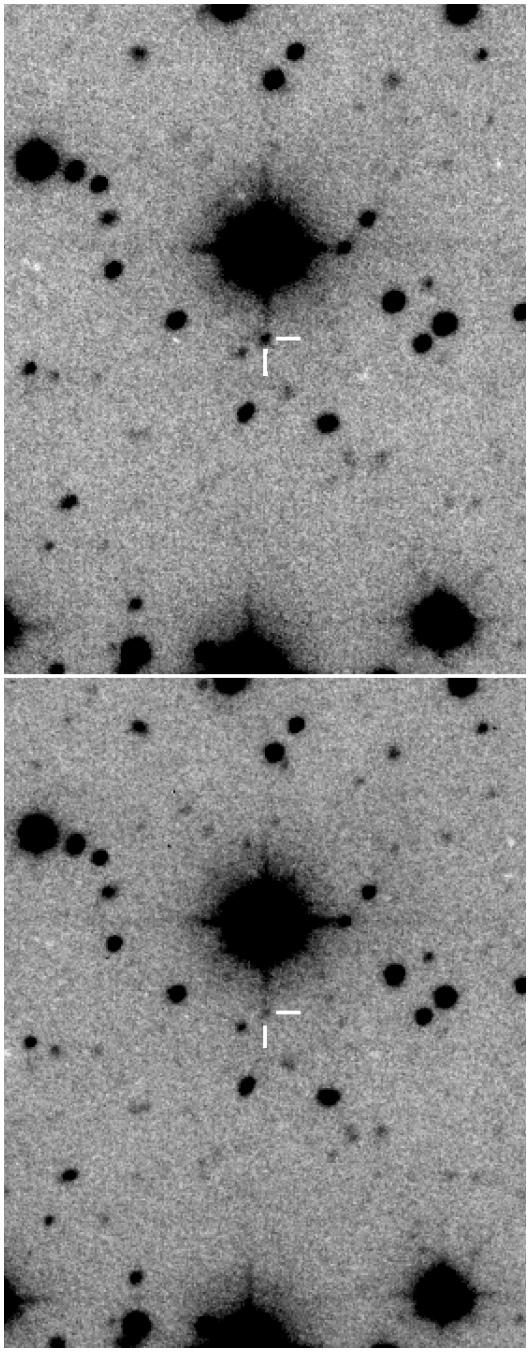

Figure 3.1: Observations of J2214+3000
1′.6 × 1′.3 images of the location of J2214+3000 as reported by the ephemeris of Ransom et al. (2011), indicated by white cross-hatches. The image on the top is a composite of 10 × 600 s R-band images at phases $\phi = 0.701 \pm 0.118$ while the image on the bottom is a composite of 10 × 600 s R-band images at $\phi = 0.355 \pm 0.0818$. East is up and north is to the right.

Object	MJD	Exposure	Filters	Airmass	Telescope	Instrument	Magnitude
J1810+1744	55329	42 × 300 s	R	< 2.084	Hiltner	Echelle	(22.74, 19.63, 20.31)
	55362 ± 1	80 × 300 s	R	< 1.44	McGraw-Hill	Templeton	
	55356	9 × 300 s	R	< 1.285	Hiltner	Nellie	
	55448	64 × 100 s	R	< 2.2	Hiltner	Echelle	
	55800	6 × 300 s	R	< 1.04	Hiltner	Osmos	
	55714	30 × 120 s	V	< 1.248	Hiltner	Templeton	(23.57, 19.82, 20.52)
	55715	25 × 600 s	V	< 1.413	Hiltner	Templeton	
	55715	40 × 300 s	B	< 1.58	Hiltner	Templeton	(24.11, 19.93, 20.68)
	55797	37 × 300 s	B	< 2.64	Hiltner	Osmos	
J2215+5135	55356	3 × 300 s	R	< 1.6	Hiltner	Nellie	(19.70, 18.53, 18.94)
	55452	29 × 600 s	R	< 2.31	Hiltner	Echelle	
	55743 ± 2	55 × 300 s	R	< 1.819	McGraw-Hill	Templeton	
	55743	75 × 100 s	R	< 1.3	McGraw-Hill	Templeton	
	55747	23 × 200 s	V	<1.25	McGraw-Hill	Templeton	(20.19, 18.73, 19.27)
	55800	51 × 300 s	V	< 1.3	Hiltner	Osmos	
	55798 ± 2	96 × 300 s	B	< 1.69	Hiltner	Osmos	(20.77, 18.92, 19.62)
	55716	11 × 300 s	B	< 1.189	Hiltner	Templeton	
J1745+1017	55329 ± 1	100 × 300 s	R	< 3.11	Hiltner	Echelle	> 24.78
	55353 ± 1	125 × 300 s	R	< 2.3	McGraw-Hill	Nellie	
	55365	20 × 600 s	R	< 1.607	McGraw-Hill	Nellie	

Object	MJD	Exposure	Filters	Airmass	Telescope	Instrument	Magnitude
J1816+4510	55743	6 × 300 s	R	< 1.079	McGraw-Hill	Templeton	18.27
J2234+0944	55449	10 × 300 s	R	< 1.957	Hiltner	Echelle	> 22.69
J2214+3000	55331	2 × 300 s	R	1.233	Hiltner	Echelle	(> 23.42, 22.64)
	55363	10 × 600 s	R	< 1.305	McGraw-Hill	Templeton	
	55356	8 × 300 s	R	< 1.57	Hiltner	Nellie	
	55449	39 × 600 s	R	< 1.61	Hiltner	Echelle	
	55447	220 × 60 s	R	< 2.214	Hiltner	Echelle	
	55803	57× 300 s	B	< 2.08	Hiltner	Osmos	> 24.75
J0023+0923	55803	42 × 300 s	R	< 1.33	McGraw-Hill	Red4K	> 23.52
	55801	5 × 300 s	V	< 1.4	Hiltner	Osmos	> 23.23
	55802	40 × 300 s	B	< 1.21	Hiltner	Osmos	> 24.21
J2047+1053	55802	40 × 300 s	B	< 1.204	Hiltner	Osmos	> 24.20
	55744	20 × 300 s	R	< 1.16	McGraw-Hill	Templeton	> 22.92
	55802	36 × 300 s	R	< 1.3	McGraw-Hill	Red4K	

Table 3.1: Telescopes indicated are either the 2.4 m Hiltner Telescope or the 1.3 m McGraw-Hill telescope. Instrument specifications are listed in the text. The magnitude limits are either given as the maximum image-combined 3-σ upper limits, image-combined detections near $\phi = 0.75$, or (maximum, minimum, and quadrature) magnitude model fits for the irradiated light curves measured for J1810+1744 and J2215+5135. In the case of J1810+1744, approximately half the observations within $0.15 \leq \phi \leq 0.35$ yielded only upper limits. Since model fits are also worst at minimum flux, we note that the true maximum magnitude could be different by as much as $\Delta\text{mag} = 1$, as can be seen in Figure 4.1. In the case of J2214+3000, detections at maximum in R are reported as well as an upper-limit for the minimum null detection in both R and B, which is treated with skepticism due to source confusion as described in Section 3.1.

Chapter 4

Modeling

I show in Figures 4.1 and 4.2 the full, phase-matched BVR light curves for the optical counterparts of J1810+1744 and J2215+5135 respectively. The magnitude errors and phase-scaled observing times are indicated by the vertical and horizontal error bars respectively. Near minimum under circumstances involving cloud cover or in cases where the integrated flux over the observation was below the detection threshold for the telescope and/or the instrument, upper limits are reported.

The solid curves in each Figure are the best-fit model light curves obtained using the ELC code of Orosz & Hauschildt (2000) which tracks the visibility of the Roche lobe geometry of the system and invokes a model atmosphere with the appropriate gravitational and limb darkening at each grid point. I used the code in its "millisecond pulsar mode" which models a circularized, tidally locked system with $P_{\rm orb}$ and x specified from the radio ephemeris data as reported in Table 4.1. The ELC code allows for a point-source illumination coming from the position of the neutron star and treats the reprocessed heating of the companion as a single-iteration reflection effect.

Model atmospheres of a large range of effective temperatures are required to constrain

Figure 4.1: Phase-resolved Light Curves of J1810+1744

The upper part of the plot includes the phase-resolved light curves in B, V, and R filters for J1810+1744. Vertical error bars are the photometric uncertainties while the horizontal error bars are the exposure time for each observation. 3σ upper limits for null detections are indicated by downward pointing arrows. Best-fit PHOENIX models as reported in Table 4.1 are indicated by the solid lines with $\epsilon = 10$ the efficiency factor chosen for the model fit. The lower part of the plot shows the magnitude residuals. The dispersion of the residuals in each filter is, respectively, $\sigma_B = 0.132$, $\sigma_V = 0.083$, $\sigma_R = 0.093$ mags.

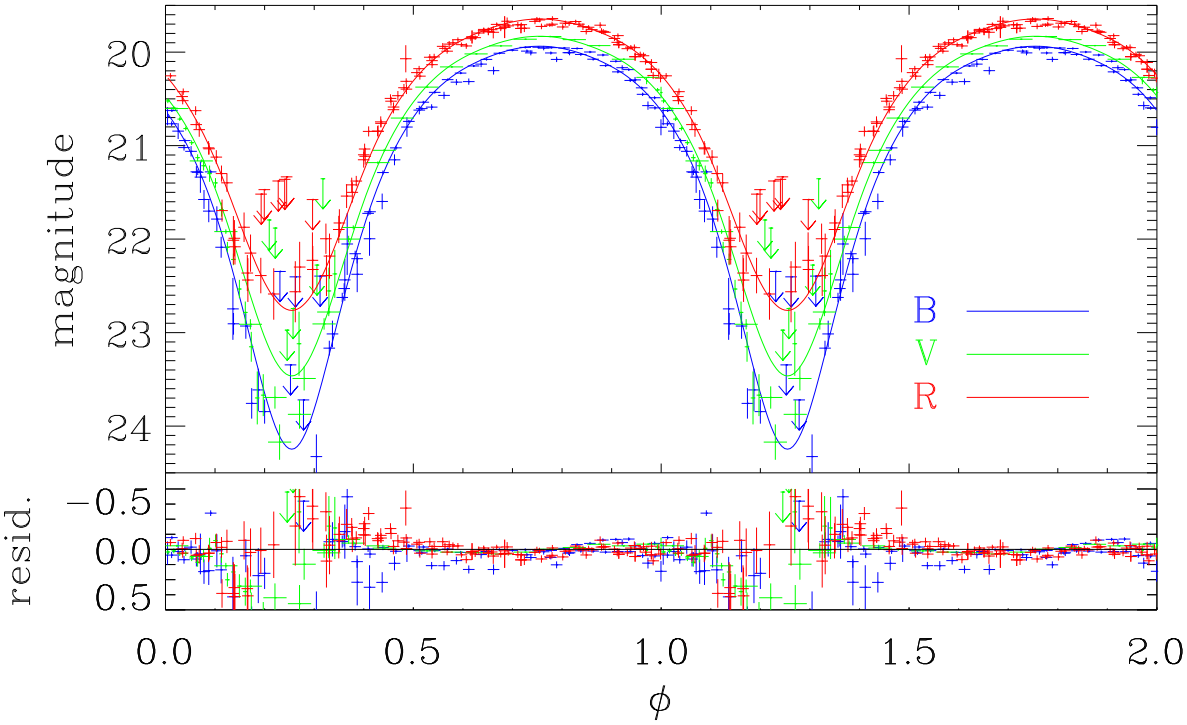

the companion profiles of these systems since the underlying star can be a cool dwarf while the irradiated side can exhibit temperatures that exceed $> 10,000$ K. I use both the NextGen (Hauschildt et al., 1999) and the newly tabulated PHOENIX atmospheres (Husser et al., 2013) to model the stellar temperatures below $< 10,000$ K while the ATLAS9 atmospheres (Castelli & Kurucz, 2004) are used to model grid cells that are at higher temperatures.

Figure 4.2: Phase-resolved Light Curves of J2215+5135

The upper part of the plot includes the phase-resolved light curves in B, V, and R filters for J2215+5135 (bottom). Vertical error bars are the photometric uncertainties while the horizontal error bars are the exposure time for each observation. 3σ upper limits for null detections are indicated by downward pointing arrows. Best-fit PHOENIX models as reported in Table 4.1 are indicated by the solid lines. The lower part of each plot shows the magnitude residuals from the best-fit model. The dispersion of the residuals in each filter is, respectively, $\sigma_B = 0.036$, $\sigma_V = 0.024$, $\sigma_R = 0.045$ mags.

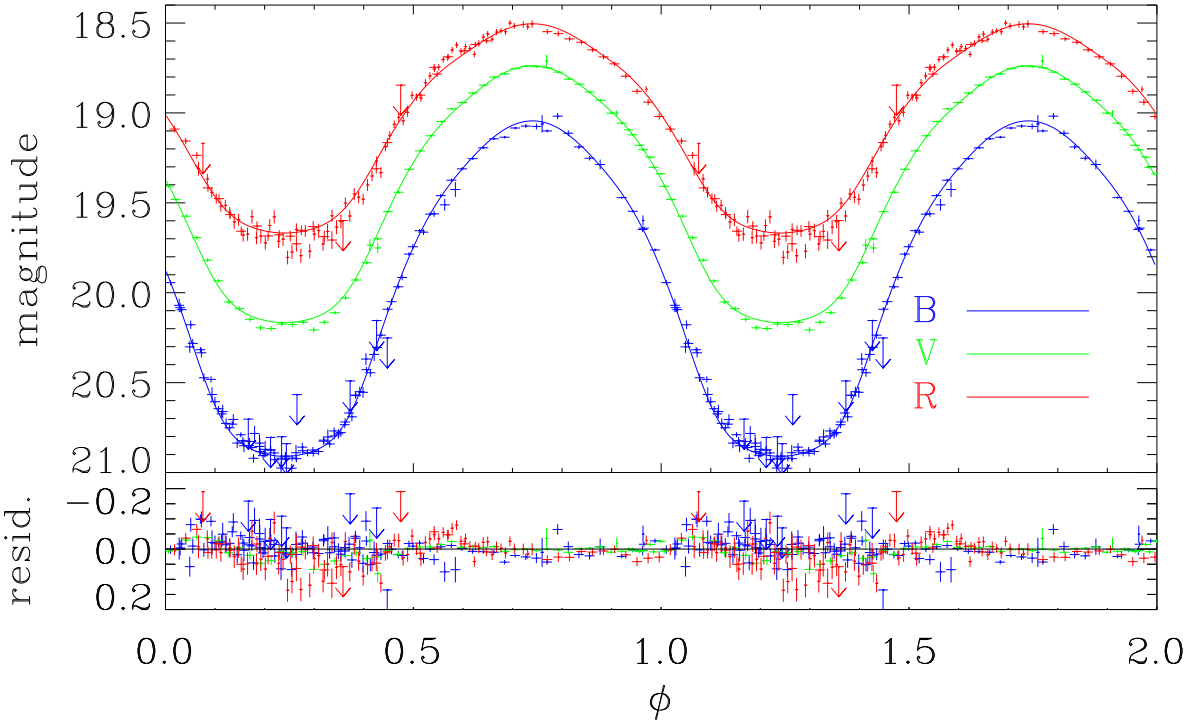

ELC allows for a customized treatment of both limb darkening and gravity darkening. For limb darkening, the classic linear law for emergent specific intensity $I(\mu)$ from a plane-parallel atmosphere was used:

$$I(\mu) = I(0)(1 - x + x\mu) \tag{4.1}$$

where μ is the cosine of the foreshortening angle of the grid element and x is the filter-dependent coefficient given by van Hamme (1993). Other limb darkening laws could be used for analysis, but such laws are generally only applied in situations where it is possible to fit for the coefficients, for example in the case of eclipsing binaries where occultation can be used to directly measure the change in intensity at the limb. Evidence exists that deviations from either the linear limb-darkening law or the standard limb-darkening coefficients could be necessary to accurately model irradiated systems or high-temperature regimes. However, there is not yet a convergence among the variety of theories that attempt to account for this and extant observations for such irradiated systems do not show consistent evidence for any one proposed modification (Alencar et al., 1999; Claret, 2007). With this important consideration in mind, the linear model is employed for this work.

The gravity darkening exponent in each element (β) is given by the equation

$$T_{\rm eff} \sim g_{\rm eff}^{\beta} \tag{4.2}$$

which relates the effective temperature of the grid element to the local effective gravity. The value was derived in the classic work of von Zeipel (1924) to be $\beta = 0.25$ and later shown by Lucy (1967) to be $\beta = 0.08$ for convective envelopes. This parametrization largely affects what underlying surface temperature structure is possible from point-to-point, and in situations such as the ones being modeled in this work, where the temperature changes dramatically across the star, the change in the exponent must be properly accounted for. This is done by implementing the temperature-dependent β given by Claret (2000).

The remaining free parameters are the following:

- *Inclination angle* (i). There are two effects seen as the inclination angle of the system increases. The largest effect is that of the line-of-sight visibility to the illuminated and nonilluminated side of the companion. Drops in flux around the

$\phi = 0.25$ phase become more significant with higher inclination angles so that an angle of $i = 90°$ gives the greatest variation from maximum to minimum light while an angle of $i = 0°$ gives no variation at all. A smaller but still measurable effect in both light curves comes from ellipsoidal variations that are also stronger at the highest inclination angles. According to Roche Lobe geometry in such tidally-locked systems, light curve ellipsoidal variations have flux peaks at phases $\phi = 0$ and $\phi = 0.5$ while their minima are at $\phi = 0.25$ and $\phi = 0.75$.

- *Mass ratio* ($Q = M_{\rm NS}/M_{\rm c}$). A prior constraint of possible mass ratios can be determined by assuming that, conservatively, neutron stars must be between $1M_{\odot} \leq M_{\rm NS} \leq 3.6M_{\odot}$, though masses at both the high end and low end are very unlikely (Baumgarte et al., 2000; Strobel & Weigel, 2001). As a higher Q (or, more precisely a higher value of $Q^3/(1+Q)^2$) implies a larger system separation to accommodate the observed orbital period, this will necessarily imply a larger inclination angle as the projected semi-major axis on the sky is fixed. To accommodate the same swing from dayside to nightside flux, the increased Q also implies a larger irradiation flux. Owing to the degeneracies between these parameters, radial velocity measurements of the companion through spectroscopic campaigns have been the usual way of constraining Q as in van Kerkwijk et al. (2011) or Romani et al. (2012). However, in the case of J2215+5135, the light curve is measured well enough to give model constraints on Q and i that only permit a narrow range of neutron star masses as discussed in Section 4.2.

- *Effective temperature* ($T_{\rm eff}$). The underlying atmospheric structure of the star is parameterized by a single intensity-weighted mean effective temperature that, absent an irradiative heating effect, constrains the observed magnitude variations to first order. Color constraints can be used to obtain distance estimates, but I consider such constraints only after the model fits were made owing to degeneracies with reddening effects. (See Section 4.2.) The overall tempera-

ture structure of the star is significantly altered when an irradiation heat source is present, meaning that the effective temperature of the star as given by the observationally-based blackbody calculation $T = (L\sigma^{-1}A^{-1})^{1/4}$ is higher than the model effective temperature. The primary difference between the PHOENIX and NextGen models are that best-fit PHOENIX models occur at approximately $\Delta T_{\rm eff} \sim 200$ K hotter than the NextGen models.

- *Irradiation efficiency* (ϵ). Owing to the fact that the ELC code was developed to model X-ray binary systems, this parameter is realized in ELC as a combination of "X-ray luminosity" (L_x) modeled to emanate from a point source located at the position of the neutron star and the bolometric albedo of the reflection effect a that is dependent upon the response of a stellar atmosphere to an irradiation source. Typically, convective atmospheres yield a reflection effect albedo of $a \sim 0.5$ while radiative atmospheres have an albedo $a = 1.0$ (Ruciński, 1969). Since this albedo is due entirely to the conditions of the envelope (convective envelopes are constrained by the condition of adiabatic temperature gradients while radiative envelopes are constrained by radiative flux equilibrium), the ELC code cannot distinguish between different $aL_x =$ constant models without more information as to the incident flux or the detailed envelope structure. The only meaningful observable constraint applicable then is a comparison of the irradiation necessary with the spin-down luminosity of the pulsar, which I give as the irradiation efficiency

$$\epsilon = \frac{aL_x}{L_{\rm SD}} = aL_x \frac{P_{\rm rot}^3}{4\pi^2 I \dot{P}_{\rm rot}}. \tag{4.3}$$

  The assumption that $\epsilon \leq 1$ is shown to be problematic for J1810+1744 as I discuss in Section 4.1.

- *Roche lobe filling fraction* ($f_{\rm Roche}$). A constraint on the size of the secondary, this parameter affects ellipsoidal variations and the $\log g$-dependent gravity darken-

ing effects for a known mass ratio (Q). Indeed, for a given i and Q, $f_{\rm Roche}$ and ϵ are both strongly constrained by the particular shape of the observed light curve at its brightest due to a competition between the heating effects that are flux-enhanced at $\phi = 0.75$ and the ellipsoidal variations that are flux-suppressed at $\phi = 0.75$. In highly irradiated cases, observations at minimum are needed to be able to constrain the filling factor as the relative signal from the ellipsoidal variations becomes more difficult to detect on a dayside increasingly dominated by irradiated flux. Other black widow systems are measured to be very close to filling their Roche lobes, (Reynolds et al., 2007; Romani et al., 2012; Breton et al., 2013) consistent with the wind-driven outflows generally considered necessary for radio eclipses (Eichler & Gedalin, 1995) and binary evolution scenarios (Chen et al., 2013). Additionally, transitioning redbacks such as J1023+0038 and J18245–2452 must satisfy the Roche-lobe overflow condition $f_{\rm Roche} = 1$ in order for accretion to happen.

- *Phase shift* ($\Delta\phi$). While the orbital parameters including the phase-timing are set by the radio data, it is possible that the heating of the secondary is offset by a certain amount due, for example, to an angular offset between the orbital relationship between the stars and the location of the stand-off shock.

In addition to the above fitted parameters, derived parameters of interest can be calculated for each model including the masses of each component using Equation 2.1, the neutron-star facing temperature which, assuming a blackbody, follows the equation

$$T_{\rm hot} = \left(T_{\rm eff}^4 + \frac{\epsilon L_{\rm SD} \sin^2 i}{4\pi \left(x(1+Q)\right)^2 \sigma} \right)^{1/4}, \tag{4.4}$$

and the predicted semi-amplitude of the radial velocity curve given by

$$K = 212.9 \sin i \left(\frac{M_{\rm NS}}{P_{\rm orb}(1+1/Q)^2} \right)^{\frac{1}{3}} \text{ km s}^{-1} \tag{4.5}$$

Table 4.1: System Parameters

Parameters Observed and Derived from Radio Observations

parameters	J1810+1744	J2215+5135
$P_{\rm rot}$ (ms)	1.66	2.61
$\dot{P}_{\rm rot}$ (10^{-20})	0.46	2.34
DM (pc cm^{-3})	39.66	69.19
$P_{\rm orb}$ (h)	3.556087	4.140046
T_0 (MJD)	55130.048136022	55186.164695228
x (lightsec)	0.095	0.468

ELC Model Parameters

	NextGen	PHOENIX	NextGen	PHOENIX
i ($^\circ$)	56.75 ± 2.25	54.75 ± 2.75	$51.7^{+2.3}_{-1.5}$	$51.6^{+2.7}_{-2.1}$
Q	30 ± 7	29.5 ± 6.5	$5.7^{+0.3}_{-0.15}$	6.2 ± 0.25
$T_{\rm eff}$ (K)	4525 ± 175	4425 ± 225	3925 ± 20	3790^{+35}_{-25}
ϵ	10.4 ± 5.4	7.9 ± 4.7	0.083 ± 0.001	
$f_{\rm Roche}$	1.000 ± 0.007		1.000 ± 0.008	
$\Delta\phi$	$4.8 \times 10^{-3} \pm 9 \times 10^{-4}$		$-9.5 \times 10^{-3} \pm 5 \times 10^{-4}$	

Parameters Derived from Model Fits

	NextGen	PHOENIX	NextGen	PHOENIX
$M_{\rm NS}$ ($M_\odot$)	1.0 to 3.6		$1.97^{+0.08}_{-0.05}$	$2.45^{+0.22}_{-0.11}$
$M_{\rm c}$ ($M_\odot$)	0.0710 ± 0.0273	0.0735 ± 0.0285	$0.345^{+0.008}_{-0.007}$	0.396 ± 0.045
$T_{\rm hot}$ (K)	$14\,500 \pm 1000$	$13\,500 \pm 1100$	5073^{+17}_{-26}	4899^{+34}_{-23}
K (km s^{-1})	421 ± 98	414 ± 91	338^{+17}_{-9}	367 ± 15

Table of system parameters for J1810+1744 and J2215+5135 obtained from the radio data, best-fit to the ELC model using either NextGen or PHOENIX atmospheric models, and derived on the basis of the fits. Reported uncertainties were found by computing the χ^2 statistic and finding the $\Delta\chi^2 = 1$ ranges for each individual parameter. In the case of $\Delta\phi$, the NextGen and PHOENIX modeling gives the same fit because these parameters are affected only by the orientation with respect to line of sight rather than the specific Roche lobe geometry or irradiation environment. Additionally, for J2215+5153, the ϵ and $f_{\rm Roche}$ values exhibit the same constraints regardless of the model atmosphere used. In the case of J1810+1744, $f_{\rm Roche}$ was similarly constrained, but since no best-fit was possible, the reported range for neutron star masses was assumed as a prior. $\Delta\chi^2 = 1$ limits on i, Q, $T_{\rm eff}$ were then found for each ϵ-value and collated to give the limits presented here. The range of the other three derived parameters were collated on a similar basis. Constraints on ϵ values are shown as to which values permit χ^2 fits in assumed mass range.

where $M_{\rm NS}$ is measured in solar masses and $P_{\rm orb}$ is measured in days.

For both objects, I searched for and obtained best-fit models using a variety of methods including a genetic algorithm search and a grid search based on the χ^2 statistic. I was successful in finding a best-fit χ^2 minimum when varying all six parameters for J2215+5135 for which $\Delta\chi^2$ confidence intervals were then calculated. On this basis, the best-fit parameters are tabulated in Table 4.1. Best-fit values for J1810+1744 could only be ascertained for $\Delta\phi$ and $f_{\rm Roche}$, while limits on i, Q, and $T_{\rm eff}$ could only be placed on the basis of assumed prior probabilities for $M_{\rm NS}$ and ϵ. Indeed, the global best-fit models for J1810+1744 were beyond the limits of physically plausible neutron star masses and amounts of irradiation. I discuss this issue more in Section 4.1 while Table 4.1 lists either the best-fit model parameters and confidence intervals based on $\Delta\chi^2 = 1$, or, for the parameters of J1810+1744 where no best-fit was possible, the range of likely values given the condition that $1.0M_\odot \leq M_{\rm NS} \leq 3.6M_\odot$.

4.1 J1810+1744 Model Fits

Without relaxing either the condition of $\epsilon \leq 1.0$ or $M_{\rm NS} > 1.0M_\odot$, neither of the NextGen nor the PHOENIX models are able to reproduce the observations of the B and V bands at minimum $\phi = 0.25$. If I impose a hard-limit of $\epsilon < 1$ on our fitting routine, I find all physically plausible neutron star masses $M_{\rm NS} > 1M_\odot$ excluded at projected 3σ ($\Delta\chi^2 < 9$ for the projection into the single parameter). Allowing the efficiency to float results in the best-fit model with the lowest reduced $\chi^2/\nu = 1.7$ at $\epsilon \sim 100$ and similarly implausible neutron star masses of $M_{\rm NS} > 10M_\odot$. I therefore propose that 1) it is likely that $\epsilon > 1$, and 2) in spite of χ^2 values favoring higher efficiencies because $\Delta\chi^2/\Delta\epsilon < -9$ along a best-fit model path from $\epsilon = 1$ to $\epsilon = 31.6$ shown in solid green in Figures 4.3 and 4.4, the physical implausibility of the highest ϵ values means that the fitting routine alone cannot distinguish between different

Figure 4.3: J1810+1744 Best-Fit Models Using PHOENIX Model Atmospheres

J1810+1744 best-fit models using the PHOENIX model atmospheres in the Q vs. i. The solid green line traces the location of the best-fit models for efficiencies in order from bottom to top of the plot as $\epsilon = (1.0, 1.3, 1.6, 2.0, 2.5, 3.2, 4.0, 5.0, 6.3, 7.9, 10.0, 12.6, 15.8, 20, 25.1, 31.6)$ with the points indicated with crosses. Black, dark gray, and light gray respectively correspond to the $\Delta\chi^2 = 1, 4,$ and 9 contours projected for efficiencies of $\epsilon = 1, 4.0, 10.0$. Additionally, evenly-spaced lines of constant $M_{\rm NS}$ are shown in dotted-blue while lines of constant $M_{\rm c}$ are shown in dashed-red with certain associated numerical values labeled. Note that the $\Delta\chi^2 = 1$ projection of these regions onto Q, i, $M_{\rm NS}$, and $M_{\rm c}$ are the uncertainties quoted in Table 4.1.

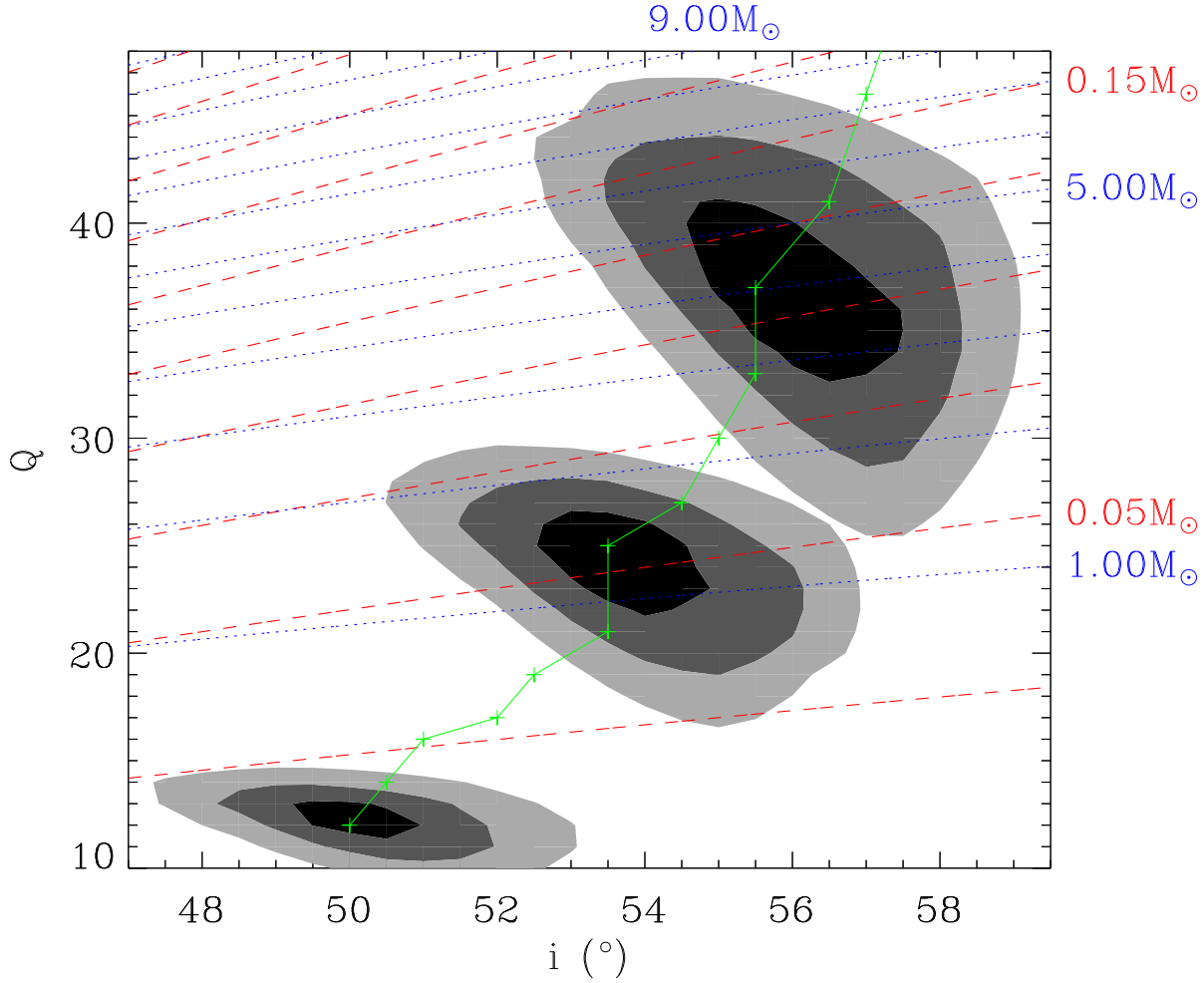

Figure 4.4: J1810+1744 Best-Fit Models Using NextGen Model Atmospheres

Same as Figure 4.3 except using the NextGen model atmospheres. Contours plotted are for the values $\epsilon = 1, 5.0, 12.6$.

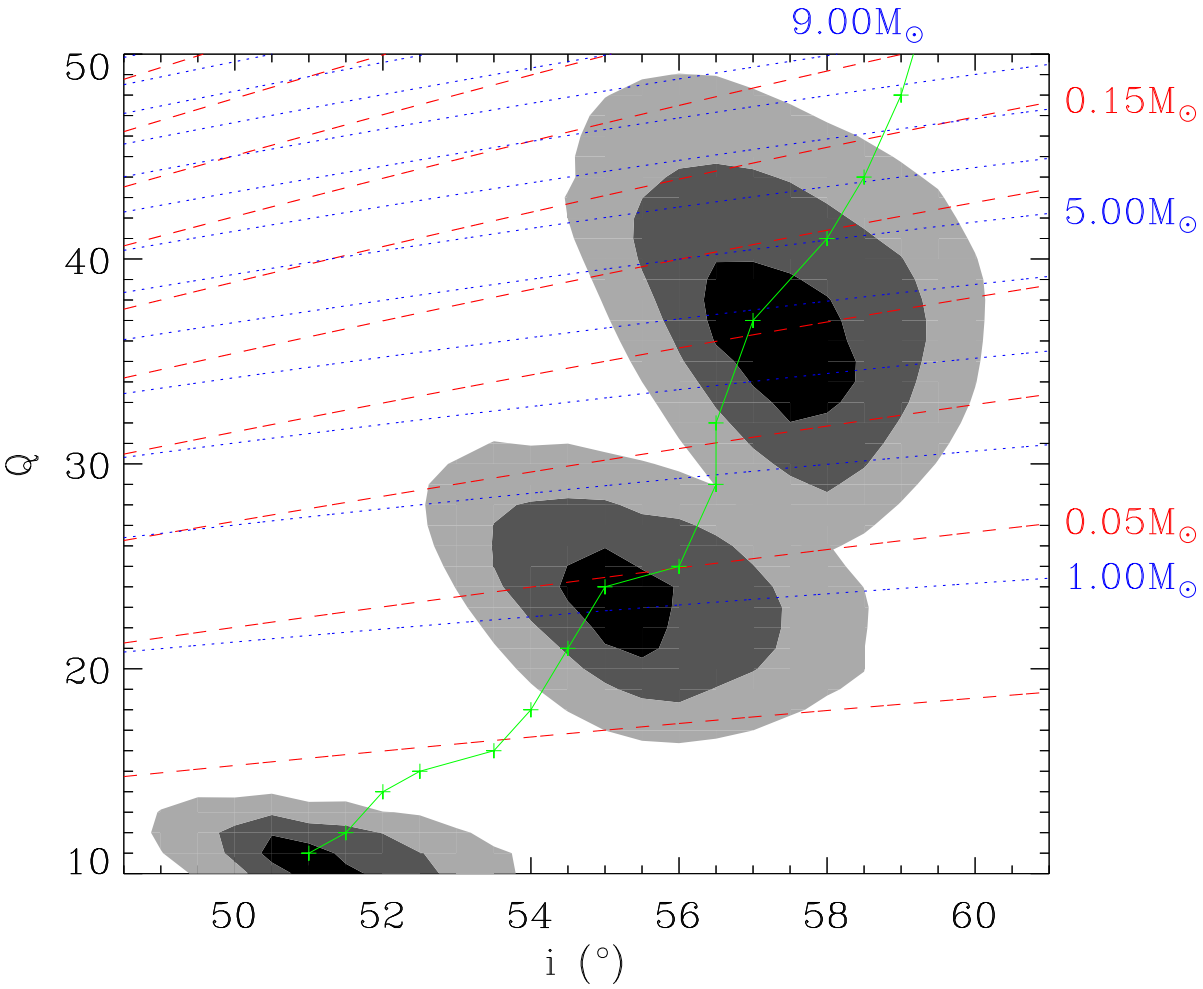

efficiencies.

However, other system parameters are fit to a high degree of confidence as demonstrated in Table 4.1. For example, I find that the companion to J1810+1744 is filling its Roche Lobe to within a degree of uncertainty of $\Delta f_{\rm Roche}/f_{\rm Roche} < 1 \times 10^{-3}$. This fit applies regardless of which efficiency I choose on the basis of the shape of the light

curve near minimum since its precise slope is dependent on matching the visibility to the hot side of the companion with a steepened drop in flux due to the minimum in the ellipsoidal variations. Essentially, without allowing for a nearly filled Roche lobe, the light curve's precipitous drop at $\phi = 0.25$ is too steep for any point illuminated sphere. As Romani et al. (2012) point out in their fit for a "flyweight" mass companion to the millisecond pulsar J1311–3430, allowing for a smaller-in-extent hot-spot on the illuminated side could potentially resolve tensions in the model fits, but rather than add this additional set of free parameters I use the simplest irradiation model and leave improvements in modeling the possible temperature structure for future investigations.

A phase shift corresponding to a 62 second delay from the measured radio-ephemeris phase calculated by means of Equation 3.1 is robustly measured and I discuss the implications of this particular result in more detail in Section 5.1.2.

Because our best-fit model lies outside the range of plausible neutron star masses, I report limits in Table 4.1 that reflect trials taken at varying values of ϵ chosen on the basis of a simple Monte Carlo bootstrap of the χ^2 statistic when varying ϵ. For each efficiency, a best-fit minimum χ^2 in i, Q, and $T_{\rm eff}$ is ascertained, the i- and Q-locations of which are plotted in green in Figures 4.3 and 4.4. The value of ϵ was then varied higher keeping the other parameters constant to find $\delta\chi^2 = 9$ and the procedure was repeated to populate the list given in the caption of Figure 4.3. Because the χ^2 fits strongly favor higher efficiencies, simply imposing a prior constraint on the neutron star mass would return the highest neutron star mass considered. I instead calculate the areas of parameter space where, for each slice in ϵ, $\Delta\chi^2 \leq 1$ overlaps with areas of parameter space corresponding to $1M_\odot \leq M_{\rm NS} \leq 3.6M_\odot$. This gives limits on the possible values of ϵ. Additionally, limits on i, Q, and $T_{\rm eff}$ are given as the maximum extent that $\Delta\chi^2 = 1$ around specific values of ϵ give with the additional neutron star mass constraints. To illustrate the character of this peculiar likelihood function, I have also plotted in Figures 4.3 and 4.4 certain representative

$\Delta\chi^2$ confidence intervals around three arbitrarily chosen values of ϵ for both the NextGen and PHOENIX models. While limits I place on system parameters overlap between the NextGen and PHOENIX atmospheres, I separately report ranges of i, Q, $T_{\rm eff}$, and ϵ for the two models in Table 4.1 to illustrate how the model fits change under the influence of these different sets of assumptions.

Assuming no reddening, the $B-V=0.158$ color at maximum reported in Table 3.1 corresponds to a color temperature lower bound of $T_{\rm color} > 8000$ K (Flower, 1996) consistent with the reported blackbody results of Breton et al. (2013). Correcting for the interstellar reddening using the extinction values for each filter given by Schlegel et al. (1998) of $A_B = 0.486$, $A_V = 0.368$, and $A_R = 0.291$ while taking into consideration the systematic uncertainty in the zero-point of the magnitude scale yields a $B-V = 0.02\pm0.1$ that is consistent with $T_{\rm color} = 9600 \pm 1500$K for solar metallicities. I note that because the integrated profile of the companion varies strongly with longitude, the color temperature should be cooler than the maximum $T_{\rm hot} \approx 14,000$ K reported in Table 4.1 owing to the visibility of cooler and redder locations on the surface even at maximum. Solving for the distance to J1810+1744 is dependent on which efficiency is chosen. For the system sizes examined in Figures 4.3 and 4.4, a range of distances from 500 ± 250 pc for the smallest system to 5 ± 2.5 kpc for the largest system is calculated; encouragingly, these values bracket the 1.9 kpc distance obtained when using the observed dispersion measure and the NE2001 Galactic free electron density model of Cordes & Lazio (2002).

Breton et al. (2013) describe model fits for J1810+1744 as indicating an inclination angle of $i = 48^\circ \pm 7^\circ$ and a blackbody temperature profile ranging from 4600 to 8000 K. They reject numerical light curve modeling in part due to their best-fit model yielding a physically implausible efficiency of $\epsilon = L_{x/}L_{\rm SD} = 1.5$ which is lower than the efficiencies that I find are best fit. Their lower inclination angle also accommodates a greater range of possible $f_{\rm Roche}$, though their results were consistent with $f_{\rm Roche} = 1$.

4.2 J2215+5135 Model Fits

In contrast to J1810+1744, the counterpart to J2215+5135 is better-measured photometrically throughout its orbit, especially at minimum. This allowed me to fit the system parameters with greater certainty than for J1810+1744 and the fits are not further complicated by implausible energetics or neutron star masses. As reported in Table 4.1, the uncertainties on the fit system parameters for both the NextGen and PHOENIX atmospheres (in both cases, reduced $\chi^2/\nu = 1.5$) are consistent, except for the $T_{\rm eff}$ which are only consistent to within their $\Delta\chi^2 = 9$ contours. This difference in $T_{\rm eff}$ causes a discrepancy in $T_{\rm hot}$ and corresponds to shifts in parameter space roughly orthogonal to the direction of lines constant mass in the Q vs. i planes plotted in Figures 4.5 and 4.6. Therefore, the derived parameters, $M_{\rm NS}$, $M_{\rm c}$ are also inconsistent to a similar degree while K values for both models are consistent to within each other's $\Delta\chi^2 = 1.5$ contours.

As in the case of J1810+1744, the companion to J2215+5135 is found to be filling its Roche lobe to a high degree of certainty $\Delta f_{\rm Roche}/f_{\rm Roche} < 1\times10^{-3}$ due to the particular shape that its light curve exhibits with flattening at maximum and deepening at minimum being the most noticeable effects of the ellipsoidal variations. In this case, the precise shape is also enough to constrain the efficiency factor to a high degree of precision and it is consistent with the $\epsilon < 1$ limits. The phase shift measured for this system corresponds to the observed light curve leading the expected phase derived from the radio ephemeris by 144 seconds. I discuss this result in more detail in Section 5.1.2.

In effect, the only free parameters for this system are i, Q, and $T_{\rm eff}$, so I calculated the χ^2 statistics around the best-fit values for these and then projected into the Q vs. i plane in Figures 4.5 and 4.6 where I show the $\Delta\chi^2 = 1, 4,$ and 9 contours along with lines of constant inferred mass of the neutron star and the companion. The mass I find is comparable to that found in other black widow and redback pulsar systems

Figure 4.5: J2215+5135 Best-Fit Models Using PHOENIX Model Atmospheres

J2215+5135 confidence regions around the best-fit using the PHOENIX model atmospheres. Black, dark gray, and light gray respectively correspond to the $\Delta\chi^2 = 1, 4,$ and 9 contours projected into the Q vs. i plane. Additionally, evenly-spaced lines of constant $M_{\rm NS}$ are shown in dotted-blue while lines of constant $M_{\rm c}$ are shown in dashed-red with certain associated numerical values labeled. Note that the $\Delta\chi^2 = 1$ projection of these regions onto Q, i, $M_{\rm NS}$, and $M_{\rm c}$ are the uncertainties quoted in Table 4.1.

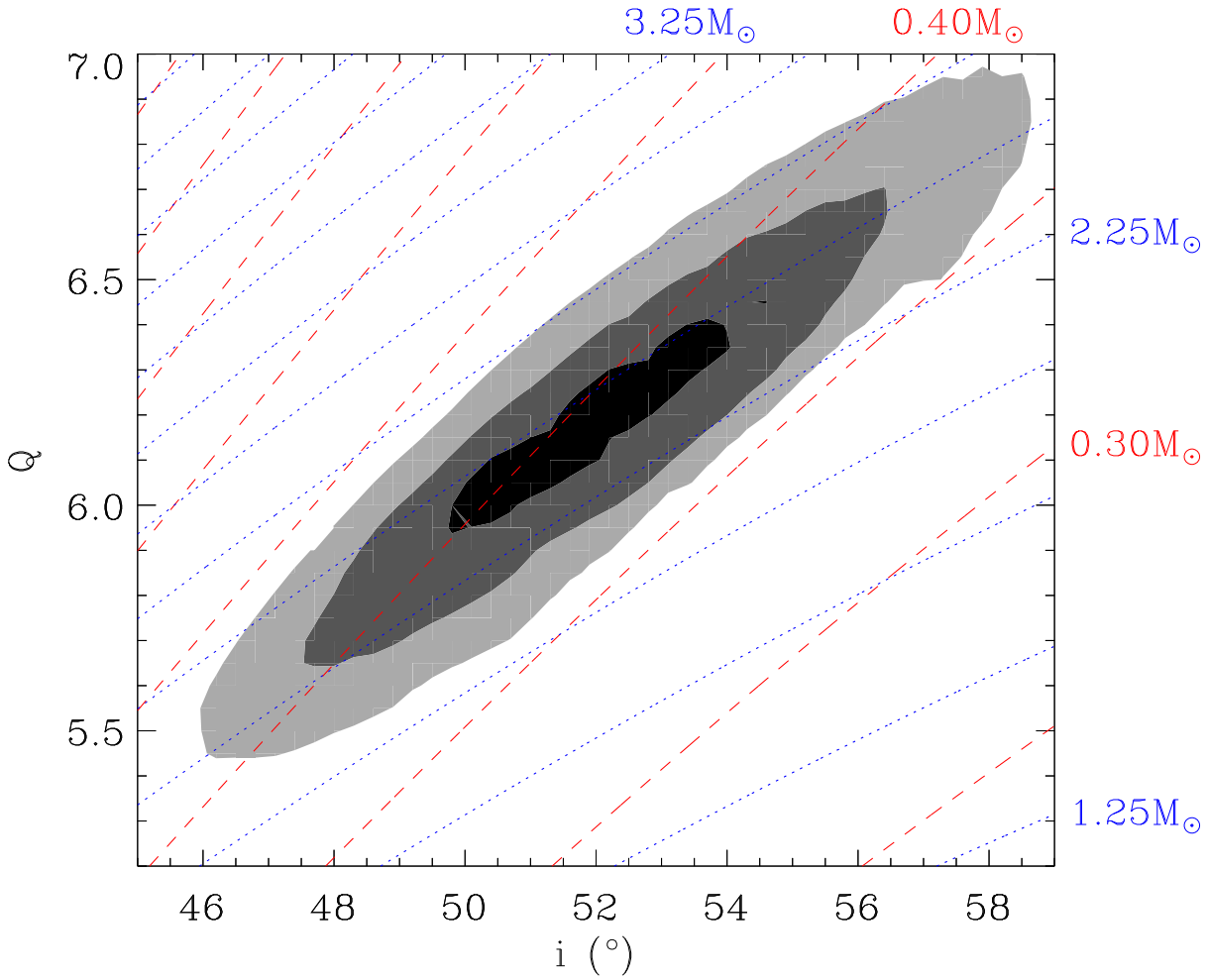

(Romani et al., 2012; van Kerkwijk et al., 2011, e.g.), with the unique feature that this determination is done without radial velocity data. This is possible because although the signal due to irradiation dominates the light curve observed, the particular shape

Figure 4.6: J2215+5135 Best-Fit Models Using NextGen Model Atmospheres

Same as Figure 4.5, but for NextGen model atmospheres (bottom).

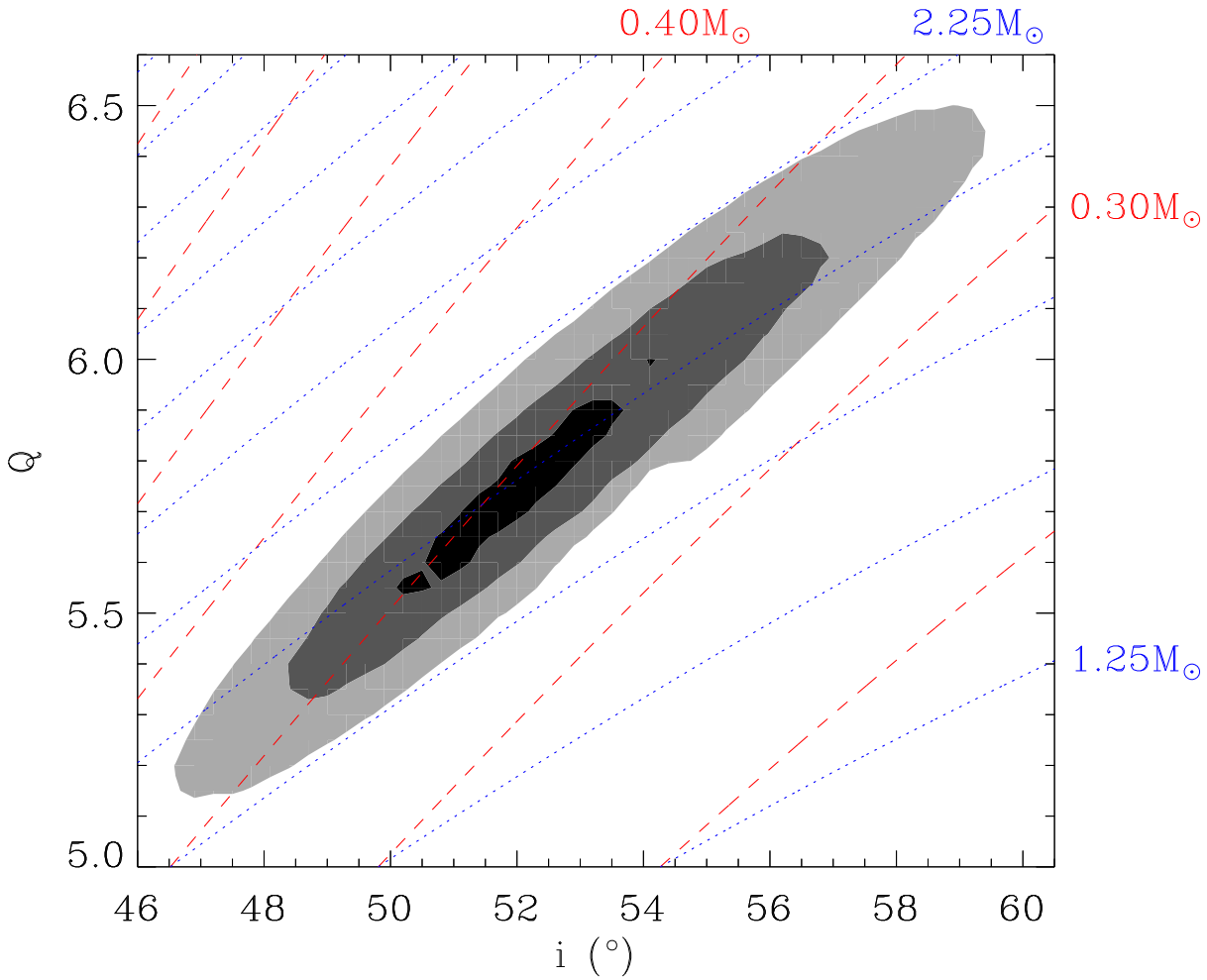

of the light curve is different than what would be expected from a point-source illuminated spherical star. It is only by taking into account the ellipsoidal variations that the light curves can be fit and, indeed, the light curve is fit by a unique combination of ϵ and $f_{\rm Roche}$.

I note that the swing in color $B-V=0.576$ to $B-V=0.188$ corresponds to color temperatures of $T_{\rm color}=6000\pm400$ K to $T_{\rm color}=7800\pm600$ K when accounting

for systematic uncertainty (Flower, 1996). This temperature corresponds with the Breton et al. (2013) best-fits but is $\sim$ 1000 K hotter than the temperatures of the model fits reported in Table 4.1. ELC modeling of effective temperature is dependent only on the variation of flux in each individual band which are simultaneously fit without determining zero-points, and so are not dependent on the observed colors. If I instead assume that the measured color temperature is the minimum possible $T_{\rm eff}$ and rerun the model fitting procedure, I find an unreasonably large neutron star mass ($M_{\rm NS} > 3.6 M_{\odot}$) at $\Delta\chi^2 = 100$. I take this as evidence that either the observed color is very aberrant or that there is an additional persistent and very blue source, for example a quiescent disk. The implications of this are discussed in more detail in Section 5.1.4.

The discordant colors would only be made worse by interstellar reddening effects. The system is in a direction where the maximum extinction values for each filter given by Schlegel et al. (1998) are $A_B = 1.256$, $A_V = 0.950$, and $A_R = 0.751$. Taking as priors the dayside temperature, effective gravity, observed size of the Roche lobe, peak apparent brightness, and extinction values along with the uncertainties on the system parameters from Table 4.1, systematic uncertainty in the zero-point calibrations, and flat priors on the extinction from the maximum to unabsorbed, a Monte Carlo simulation of possible distances was performed taking each filter independently. The results of this are shown in Figure 4.7. The distances obtained for simulations of using the measured values in each filter are $d_B = 740 \pm 190$ pc, $d_V = 1220 \pm 290$ pc, and $d_R = 1580 \pm 350$ pc. The fact that these distances are less than the 3 kpc distance calculated from the dispersion measure assuming the NE2001 Galactic free electron density model of Cordes & Lazio (2002) is evidence that there is excess light and that the excess light is bluer than that originating from just the companion.

The remaining free parameters quoted here are consistent with Breton et al. (2013), including their inclination angle of $i = 66^{\circ} \pm 16^{\circ}$ and filling factor of $f_{\rm Roche} = 0.99 \pm 0.03$. They fit ϵ to a value approximately twice what is found here, but note that if,

Figure 4.7: Distance estimates for J2215+5135

Histogram of results of 10,000 simulations given system parameter uncertainties, systematic uncertainties in magnitude calibration zero points, and flat priors on the filter extinction values. Blue is B results, green is V results, and red is R results.

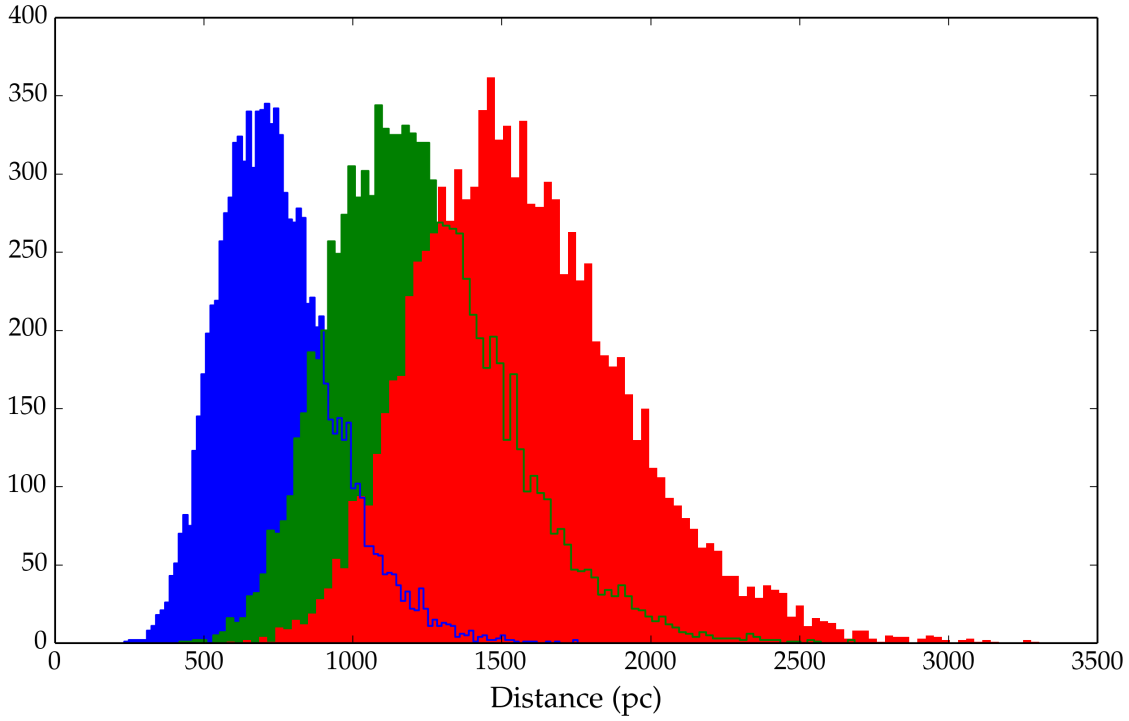

as might be expected with redbacks, the bolometric albedo due to the reflection effect $a \sim 0.5$ is consistent with a convective envelope, our value matches their reported $L_{\rm x}/L_{\rm SD} \sim 0.15$.

Chapter 5

Sequuntur

5.1 Discussion

I now consider certain novel features of our results that have not been reported in the observations and modeling of similar systems. Specifically, I discuss 1) the dependence of constraints on ellipsoidal variations and, in particular, the importance that the detection of such variations had for the model fits of J2215+5135, 2) the phase shifts present in both objects, a novel observation which has not been reported for other systems of this type, 3) the peculiarly high values of irradiance necessary to fit models of J1810+1744 which, even for completely efficient heating implies a larger incident flux on the companion than what is available from straightforward considerations of $\dot{E}_{\rm rot}$, and 4) the relatively blue colors of J2215+5135 as possible evidence for a quiescent disk in that system.

5.1.1 Ellipsoidal Variations

The model constraints I obtained for J2215+5135 were possible because the light curves were very well sampled and detailed features seen in them could be precisely

Figure 5.1: Expected Ellipsoidal Variations in J1810+1744 Modeling

Solid curves are the expected signal due to the ellipsoidal variations calculated using the same parameters as in Table 4.1 except with $\epsilon = 0$. Plotted additionally are the residuals that are present if such a signal is removed from the model light curve in Figure 4.1 with a zero point magnitude chosen to reasonably separate the light curves and the error bars propagated from the uncertainties in the flux difference. As in Figure 4.1, horizontal error bars are the exposure times scaled to the phase while the vertical error bars are the calculated magnitude uncertainties.

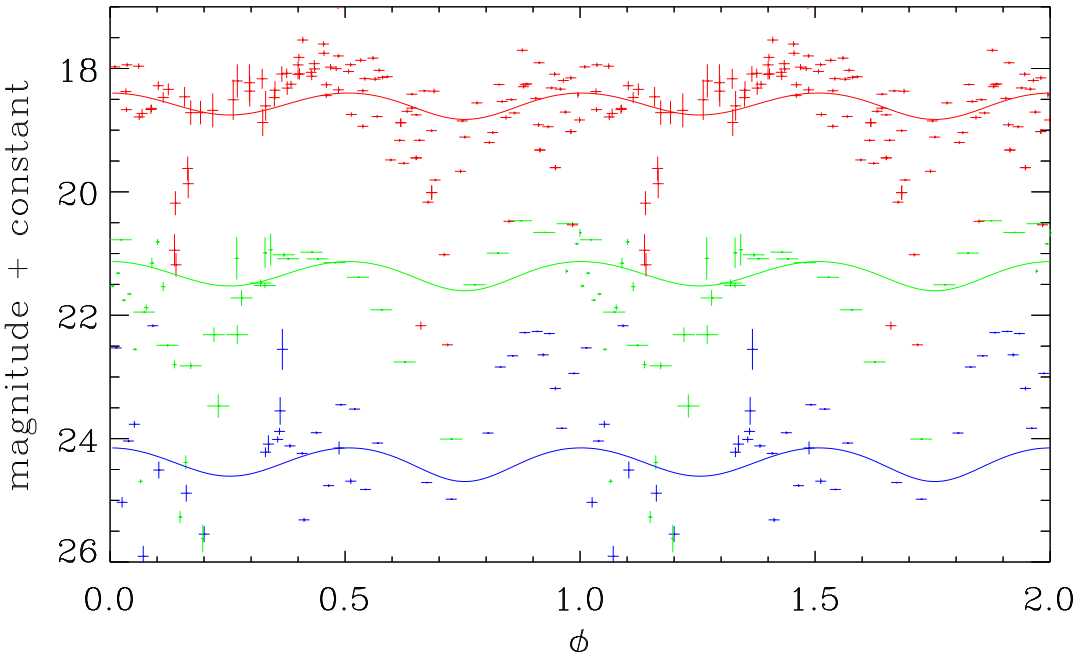

fit. This can be seen because the ellipsoidal variations are detected in the light curves of these objects. I demonstrate this by comparing the signal due to irradiated heating with the signal due to the ellipsoidal variations seen in our observations by calculating the light curve of a non-irradiated system with the same i, Q, $T_{\rm eff}$, and $f_{\rm Roche}$ and then subtracting this from the model fit shown in Figure 4.2 to obtain an "irradiation only" light curve. The flux associated with such an irradiation only light curve model is then subtracted from the data to give the residuals which can be interpreted, roughly, as the amount of signal attributable to ellipsoidal variations

Figure 5.2: Detection of Ellipsoidal Variations in J2215+5135

Solid curves are the expected signal due to the ellipsoidal variations calculated using the same parameters as in Table 4.1 except with $\epsilon = 0$. Plotted additionally are the residuals that are present if such a signal is removed from the model light curve in Figure 4.2 with a zero point magnitude chosen to reasonably separate the light curves and the error bars propagated from the uncertainties in the flux difference. As in Figure 4.2, horizontal error bars are the exposure times scaled to the phase while the vertical error bars are the calculated magnitude uncertainties.

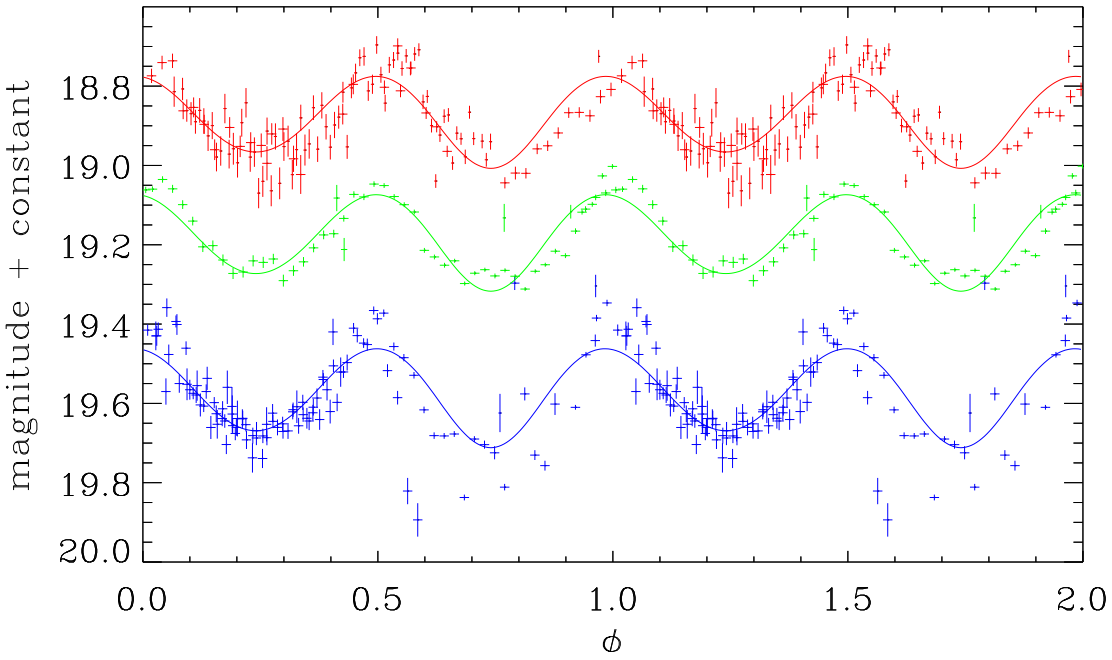

alone. This, I show in Figure 5.1. For comparison's sake, I additionally plot in that figure the light curve of a similar non-irradiated system. This is shown to indicate that ellipsoidal variations are *necessary* for fitting the light curve of J2215+5135 in that the residuals of the artificially-produced "irradiation only" match the ellipsoidal variations as the predominant second-order effect. To the extent the residuals do not match the ellipsoidal variations, the models may be failing to properly account for third-order effects such as nonisotropic heating or a lack of orbit-to-orbit stability of the stellar flux at each phase.

Ellipsoidal variations in Roche lobe geometry are constrained to a level of ~ 0.25 mag in amplitude and the amplitudes decrease for smaller values of either $f_{\rm Roche}$ or i. In principle, the ellipsoidal variation minima at $\phi = 0.25$ and $\phi = 0.75$ can be fit by tuning ϵ and $T_{\rm eff}$ to larger values to accommodate smaller variations rather than adjusting other system parameters. In contrast, the ellipsoidal variation maxima ($\phi = 0$ and $\phi = 0.5$) coincide with the part of the light curve where the heating curve's gradient is largest and thus where the flux is changing most rapidly. The shape of the light curve at these phases therefore can strongly constrain the $f_{\rm Roche}$ and essentially breaks the degeneracy. This is the primary means by which the filling factor in these light curves is constrained and, as this value is set, so are the best-fit locations in Q, i, ϵ space for J1810+1744, and Q, i space for J2215+5135 (where ϵ is strongly constrained by the less noisy signal at minimum). The fact that the ellipsoidal variations as well as the irradiation signal models are better fits to the data in J2215+5135 is confirmed in Figure 5.1. Even so, the variations in the residuals in J1810+1744 are phased with the ellipsoidal variations, and $f_{\rm Roche} = 1.0$ models are strongly preferred as the excess signal is actually larger than what is maximally possible.

5.1.2 Phase Shifts

It has been suggested that the observed heating of black widow and redback systems could be attributed to either particle or radiation fields emanating from the stand-off shock between the neutron star and the companion (Bogdanov et al., 2011). The statistically significant phase shifts seen in our fits may imply that the sinusoidal heating signal is offset from phase alignment by 62 seconds late for J1810+1744 and 144 seconds early for J2215+5135. I interpret this to mean that there is an offset between the line connecting the pulsar and the longitude of the stand-off shock from whence the heating irradiance is emitted. Future modeling of the irradiation of short period binary millisecond pulsars should include both offsets and extended emission

geometries given this and the issues outlined in Section 5.1.3.

While statistically significant in our model fits, the hypothesis that these shifts are due to offsets in source heating should be, in principle, testable if the ellipsoidal variations are observed because that signal should be in phase with the radio ephemeris measured T_0. Unfortunately, refitting the residuals in Figure 5.1 did not result in a statistically significant difference in the phase shift, though the increased uncertainty in those fits does not rule out the hypothesis that the phase shift is due to heating offsets.

5.1.3 Irradiation in J1810+1744

I find evidence that the received irradiation implied from the heating curve of J1810+1744 is in excess of the typical value given for the spin-down luminosity. According to our model fits presented in Figure 4.3, the best-fit luminosities lie between $4.0 < \epsilon < 10$ for models that allow for best-fit neutron star masses between $1.0M_{\odot} \leq M_{\rm NS} \leq 3.6M_{\odot}$. This is consistent with the best-fit models quoted by Breton et al. (2013) for this object.

While such efficiencies superficially seem to be in excess of what would be permitted given the energy budget afforded by the canonical spin-down luminosity calculated for J1810+1744, there are some straightforward arguments that could lead us to consider that a larger amount of incident radiation from the neutron star onto the companion can be accommodated. In particular, the assumption that the irradiation originating with the neutron star is isotropic is likely to be inaccurate. For example, MHD simulations of outflows (Komissarov & Lyubarsky, 2004) and the characteristics of the termination or stand-off shock associated with pulsar winds (Pétri & Dubus, 2011; Sironi & Spitkovsky, 2011) indicate that while the winds are likely axisymmetric, they are not likely to be spherically symmetric. If the energy released by the pulsar is preferentially emitted at a bright equatorial stand-off shock, the heating of the companion would be in excess of what would be naively calculated assuming an

isotropic point source emanating from the neutron star.

5.1.4 Evidence for a Quiescent Disk in J2215+5135

The tension between the color temperature observed for J2215+5135 and the model temperature I take as evidence for an additional source. Such a source would have to be comparable in luminosity to the companion star, but significantly hotter. Additionally, since the data indicate photometric stability even over many orbits, the discrepant source must be relatively stable in temperature and luminosity. As seen in Section 4.2, the discrepancy in the distance estimates from the peak brightness in each filter can be taken as evidence that there is additional light in the system, and that the spectrum of this light is skewed towards the blue.

J2215+5135 is in a class of redback objects which compare to J1023+0038, the so-called "missing link" pulsar, that was observed to transition from an accretion-powered to a rotation-powered pulsar while also losing the emission features associated with its accretion disk (Wang et al., 2009). However, as accretion onto the neutron star ends, it is possible that a quiescent disk could remain between the companion and the light cylinder of the neutron star (Ekşİ & Alpar, 2005). Is there any additional evidence for such a feature? Breton et al. (2013) report serendipitous measurements of the system with the *Swift* UVOT instrument measured in the uvw1-band from 23.531 ± 0.561 at $\phi = 0.0572$ to 21.930 ± 0.325 at $\phi = 0.4216$ which show a statistically significant modulation in phase with the optical observations, but with large enough uncertainties that a persistent disk could be possible as an additional component. Additionally, Gentile et al. (2014), X-ray observations were made of J2215+5135 and minima in the light curves were found around $\phi = 0.25$ for both hard and soft X-rays. In my proposal, this modulating X-ray signal could be indicative of the X-ray bright disk being eclipsed as the companion passes between the neutron star and our line-of-sight. However, an alternative explanation could also be that the X-rays are

coming from a shock close to the companion star, which would not require there to be an accretion disk. The photon statistics are not enough to draw a definite conclusion as to the source of the X-rays.

Given $\eta = A_c/A_d$, the ratio of the visible surface area of the companion at phase $\phi = 0.75$ (A_c) to the visible surface area of any disk present in the system (A_d), a blackbody temperature for the disk is $T_d = [T^4_{\rm color} + \eta(\, T^4_{\rm color} - T^4_{\rm hot}\,)]^{1/4}$. Assuming no reddening, $\eta = 1$ implies a disk temperature of $T_d = 9000$ K, while correcting for the full $E_{B-V} = 0.372$ reddening in that direction (Schlegel et al., 1998) implies a temperature of $T_d = 19,000$ K. Alternatively, the same argument made for observations at the light curve minimum gives a temperature of the disk of $T_d = 7000\ K$ or $T_d = 9000\ K$. However, it is important to note that color temperature is very sensitive to zero-point calibration and the systematic uncertainty in our calibration leaves a very wide range of permissible disk characteristics.

A reinterpretation of the light curves in Figure 4.2 would be necessary if a maximally brightest possible disk is assumed. The flux from such a disk would dominate at minimum, and the relatively constant flux seen in all bands from phases $\phi = 0.1$ to $\phi = 0.3$ would be attributed entirely due to the disk light. To test such a hypothesis, I reran ELC assuming that the flux from $\phi = 0.1$ to $\phi = 0.3$ is due to a source with $\eta = 1$ and the temperature was given by the $B - V$ color temperature at minimum $T_{B-V} = 5950$ K. The best fit model under this scenario has a lower ϵ, higher Q, and lower i resulting in a prohibitively high best fit $M_{\rm NS} = 3.5\ M_\odot$ for the NextGen models and $M_{\rm NS} = 4.1\ M_\odot$ for the PHOENIX models. The set of model parameters including a third light that can successfully reproduce the Figure 4.2 light curves range from the fits reported in Section 4.2 to the highest possible neutron star mass to be considered. Thus, it is possible to treat our system parameters derived without a third light as a lower bound on the mass of the neutron star. If one believes that additional light is present, then our models predict a higher best-fit mass and shift of the contours up and to the left in Figure 4.6.

The existence of such a disk in this system would imply that an expectation for similar behavior in J2215+5135 as that observed in J1023+0038 and IGR J18245–2452 with the pulsar alternating between accretion-powered and rotation-powered modes. If the object were to begin accreting, this would result in an increase in X-ray luminosity and the presence of strengthened emission lines.

5.2 Conclusions

I presented evidence that the photometric light curves observed from J2215+5135 are consistent with a neutron star of mass $2M_{\odot}$. This mass estimate based on photometry alone was possible because the light curve was sampled well enough to fit both the shape and amplitude of the heating and ellipsoidal variations. This result can be used as a prediction of what radial velocities I expect will be detected when this object is measured spectroscopically. Additionally, spectroscopic observations could be used to confirm the presence of a quiescent disk associated with this redback. If J2215+5135 is similar in type to J1023+0038, ongoing X-ray monitoring of the object will be useful in detecting if the object transitions from a rotation powered to an accretion powered system. This high-mass neutron star is readily comparable in size to the measurements of Romani et al. (2012) and van Kerkwijk et al. (2011).

In contrast, J1810+1744, the second object for which detailed light curves were obtained, was not adequately constrained by our modeling. Whether this is due to a failure of the point-source illumination model or whether it may be due to intrinsic variability of the object is not clear. Spectroscopic observations of this object will be vital in constraining the mass ratio and therefore the neutron star mass in the system.

In addition, I reported the first detection of the optical counterpart of J2214+3000 at $R = 22.64$ around the the expected phase ($\phi = 0.75$) of maximal heating.

5.3 Future Work

I hope to continue to pursue this line of inquiry by conducting systematic observing campaigns in the future that will be similar in process and go beyond the campaign outlined in this dissertation and the recently submitted paper, Schroeder & Halpern (2014). To date, only $\sim 10\%$ of the radio-confirmed binary millisecond pulsars discovered by *Fermi* LAT and the radio follow-up teams have been successfully associated with optical counterparts in the published literature, and, of those, only one has had full photometric and spectroscopic follow-up (Romani et al., 2012). Especially needed is a devoted follow-up campaign in the Southern Hemisphere, imaging Fermi LAT error boxes using ground-based telescopes – a project that has the potential to yield confirmed detections considering our success using 1-2.5m sized facilities. These detections can be made on the basis of correlating optical variations with what is expected from the period and phase information obtained from the radio data: brighter at phase $\phi = 0.75$ when the hot side of the companion is visible and fainter at phase $\phi = 0.25$ when the cold side is visible. For orbital periods on the order of hours, as shown in this work, full orbital coverage in two bands can be enough to fully constrain the inclination and, if the sampling is complete enough, color data can break certain degeneracies in the fitting algorithms to fit all unknown system parameters using photometry alone. Additionally, a number of binary and millisecond pulsars have been observed to have associated Hα bow shocks (Kulkarni & Hester, 1988; Mann et al., 1999), and therefore Hα imaging will be a natural enhancement to my photometric observing campaigns. The first major effort to conduct such a study has already begun with the work of Brownsberger & Romani (2014) where two new Hα structures associated with LAT pulsars have been discovered along with upper limits for 94 additional ones.

After detections and photometry-based model-fits are completed, spectroscopic follow-up on large ground-based telescopes should be conducted to identify the spectral type

of the companions at various orbital phases. Radial velocity curves from the follow-up can then be used to directly constrain the mass ratio of these systems and, by extension, measure as many neutron star masses at the heavier end of the spectrum as possible. X-ray observations of similar systems have revealed orbital variability and give evidence for the disk structure that may exist even when such systems are not in an accretion mode (Bogdanov et al., 2011), so additional observations and analysis using X-ray observatories, including archival data, will complement follow-up campaigns well.

With improved datasets comes the necessity for improved modeling of short period binary millisecond pulsar systems. The Eclipsing Light Curve (ELC) code of Orosz & Hauschildt (2000) has typically been used for this purpose with Breton et al. (2012, 2013) introducing modifications in a new code named "Icarus" that allow for priors such as reddening and distances to be more accurately incorporated. While this work highlights how successful modeling can be with current technology, the failure of the model to account for the observations of J1810+1744 as well as the observed phase shifts, implies that there are additional issues left unaddressed by these standard light curve models. If properly accounted for, it is possible that improved models could resolve some remaining problems and mysteries seen in this work as well as, for example, the preferred models of Romani et al. (2012) that required additional hot spots to be added to obtain adequate fits, perhaps indicating that the heating mechanism or energy transport in the companion was not well-characterized by the ELC model.

A decent interrogation and modification of some of the simplifying assumptions used in modeling and help develop next generation modeling codes may include 1) relaxing the assumption that irradiation can be modeled as a point-source illumination and 2) relaxing the assumption that grid-based model atmospheres can accurately account for the heating response of secondaries. While ELC allows for irradiative heating due to either a point source or a disk, these systems are likely heated by particles and

radiation emanating from an extended stand-off shock (Bogdanov et al., 2011) that is not a part of current codes. Adjusting models to accommodate more advanced heating geometries and comparing them to a more comprehensive data set will help answer the question, "What is the precise nature of the heating mechanisms in binary millisecond pulsar systems?" Confirming or falsifying such models requires improving the heating models and applying them to extant and future observations. Additionally, irradiated atmospheric models of hot Jupiters (Fortney et al., 2008), which have been lately applied to irradiated brown dwarfs (Beatty et al., 2013), should be incorporated into the models for the lowest mass companions observed.

5.4 Parting Thoughts

In this work, two different binary millisecond pulsars, one, J1810+1744, a black widow, and one, J2215+5135, a redback showed characteristics that may be illustrative of the features of their respective populations. While it is an extreme hazard to speculate too freely on the basis of such a small number of data points, an interesting picture has emerged over the course of writing this thesis that I would be remiss if I did not share.

The model provided by Phinney et al. (1988) of an ablating dwarf with the explicit suggestion that such a system could account for the existence of isolated millisecond pulsars (whereby the companion was completely disrupted) was considered a plausible explanation for how pulsars became recycled. Outstanding issues (e.g., Levinson & Eichler, 1991) in how accretion, which transfers material from the companion to the primary, and the tandem processes of ablation and the propeller mechanism (Alpar, 2001), which both expels material from the system, operate to provide evolutionary pathways is still an area of active research (Benvenuto et al., 2014).

The initial (Roberts, 2011) division of the eclipsing binary millisecond pulsar pop-

ulations into redback and black widow subpopulations has been enhanced by the discovery of these systems. The obvious bifurcation at ~ 0.1 $M_\odot$ is easily seen in a histogram-like plot of the distribution of possible companion masses in Figure 5.3. Explaining the dual populations is particularly tricky as certain authors (e.g., Benvenuto et al., 2014) insist that larger redbacks evolve into the smaller black widows while others (e.g., Chen et al., 2013) argue that the two populations represent two different channels of binary evolution because of differences in their geometries and irradiation efficiencies. Historic work on the subject showed connections between redback-sized progenitors and ultracompact systems (Podsiadlowski et al., 2001), which would tend to support the latter scenario, while the ongoing mass-loss observed in the system would, at least superficially, tend to support claims that redbacks evolve into black widows and then on into isolated millisecond systems.

Discoveries continue apace, and Patruno et al. (2014) has shown that the transitions of PSR J1023+0038 have continued with the system coming full cycle to having a reappeared accretion disk and increased X-ray flux. The fact that the two "missing link" objects that have been observed to switch between rotation-powered and accretion-powered modes known thus far are in the redback mass regime is perhaps not surprising since such objects are generally not degenerate, much more likely to completely fill their Roche Lobes, and are therefore prone to have episodes of higher mass loss rates that would be necessary to explain the intermittent accretion phases. In contrast, classic black widows like B1957+20 have never shown evidence of switching modes, and, I submit, this may prove to serve as yet another discriminant between the populations. It is, in part, why I have proposed that a disk may be found surrounding J2215+5135.

I conclude that the field is wide open and ripe for further study.

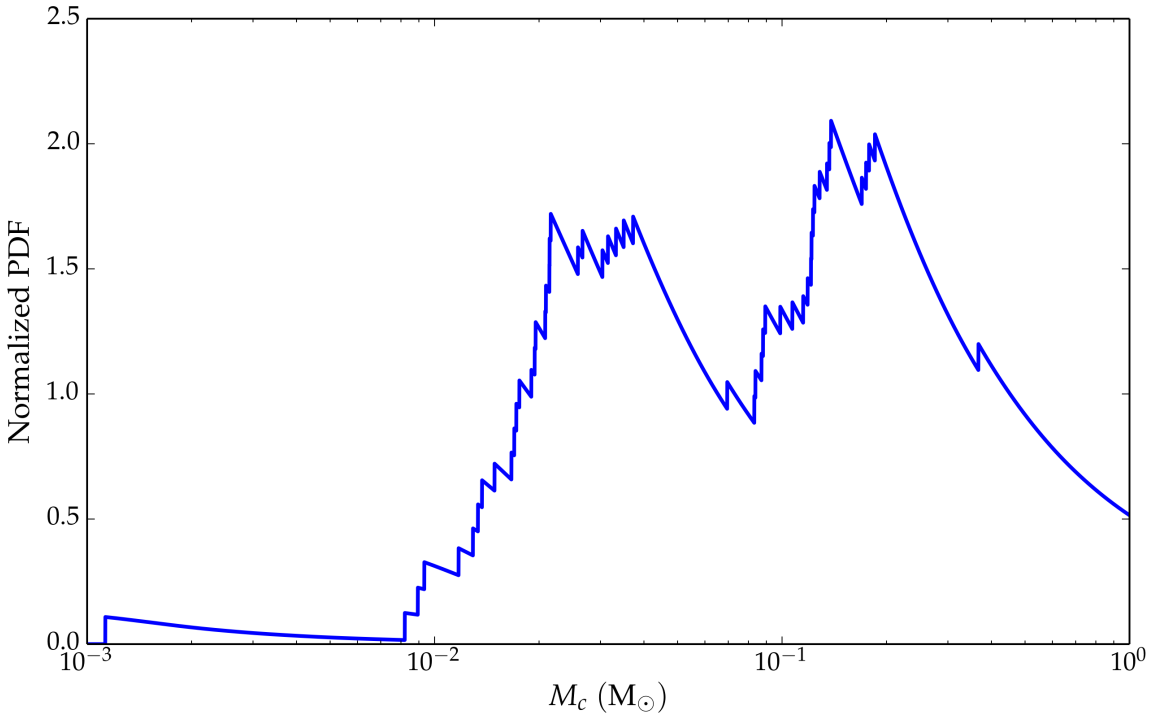

Figure 5.3: Redbacks and Black Widow Pulsars

The companion masses for all short period binary millisecond pulsars known, to date calculated by means of Equation 2.1 for each object assuming a neutron star mass of $M_{\rm NS} = 1.4$ $M_\odot$ and multiplied by the expected distribution of $\sin i$. The plot is normalized by the number of objects with $P_{\rm orb} < 1$ d for which the binary mass function is known. A bifurcation between black widow and redback masses is present as the valley at ~ 0.1 $M_\odot$.

Bibliography

Abdo, A. A., Ackermann, M., Ajello, M., et al. 2010, ApJS, 188, 405

Alencar, S. H. P., Vaz, L. P. R., & Nordlund, Å. 1999, A&A, 346, 556

Alpar, M. A. 2001, ApJ, 554, 1245

Alpar, M. A., Cheng, A. F., Ruderman, M. A., & Shaham, J. 1982, Nature, 300, 728

Angel, J. R. P., & Stockman, H. S. 1980, ARA&A, 18, 321

Applegate, J. H., & Shaham, J. 1994, ApJ, 436, 312

Archibald, A. M., Stairs, I. H., Ransom, S. M., et al. 2009, Science, 324, 1411

Avni, Y., & Bahcall, J. N. 1975, ApJ, 197, 675

Baade, W., & Zwicky, F. 1934, Physical Review, 46, 76

Backer, D. C., Kulkarni, S. R., Heiles, C., Davis, M. M., & Goss, W. M. 1982, Nature, 300, 615

Barr, E. D., Guillemot, L., Champion, D. J., et al. 2013, MNRAS, 429, 1633

Baumgarte, T. W., Shapiro, S. L., & Shibata, M. 2000, ApJ, 528, L29

Beatty, T. G., Collins, K. A., Fortney, J., et al. 2013, ArXiv e-prints, arXiv:1310.7585

Benvenuto, O. G., De Vito, M. A., & Horvath, J. E. 2014, ArXiv e-prints, arXiv:1402.7338

Bhattacharya, D., & Srinivasan, G. 1991, Journal of Astrophysics and Astronomy, 12, 17

Bhattacharya, D., & van den Heuvel, E. P. J. 1991, Phys. Rep., 203, 1

Bogdanov, S., Archibald, A. M., Hessels, J. W. T., et al. 2011, ApJ, 742, 97

Bond, H. E., White, R. L., Becker, R. H., & O'Brien, M. S. 2002, PASP, 114, 1359

Bradt, H., Rappaport, S., & Mayer, W. 1969, Nature, 222, 728

Breton, R. P., Rappaport, S. A., van Kerkwijk, M. H., & Carter, J. A. 2012, ApJ, 748, 115

Breton, R. P., van Kerkwijk, M. H., Roberts, M. S. E., et al. 2013, ApJ, 769, 108

Brownsberger, S., & Romani, R. W. 2014, ApJ, 784, 154

Burgay, M., Joshi, B. C., D'Amico, N., et al. 2006, MNRAS, 368, 283

Camilo, F., & Rasio, F. A. 2005, in Astronomical Society of the Pacific Conference Series, Vol. 328, Binary Radio Pulsars, ed. F. A. Rasio & I. H. Stairs, 147

Castelli, F., & Kurucz, R. L. 2004, ArXiv Astrophysics e-prints, arXiv:astro-ph/0405087

Chamel, N., Haensel, P., Zdunik, J. L., & Fantina, A. F. 2013, International Journal of Modern Physics E, 22, 30018

Chen, H.-L., Chen, X., Tauris, T. M., & Han, Z. 2013, ApJ, 775, 27

Chen, K. 1991, Nature, 352, 695

Chen, K., & Ruderman, M. 1993, ApJ, 402, 264

Claret, A. 2000, A&A, 363, 1081

—. 2007, A&A, 470, 1099

Cocke, W. J., Disney, M. J., & Taylor, D. J. 1969, Nature, 221, 525

Cognard, I., Guillemot, L., Johnson, T. J., et al. 2011, ApJ, 732, 47

Cordes, J. M., & Lazio, T. J. W. 2002, ArXiv Astrophysics e-prints, astro-ph/0207156

Crawford, F., Lyne, A. G., Stairs, I. H., et al. 2013, ArXiv e-prints, arXiv:1308.4956

Deller, A. T., Archibald, A. M., Brisken, W. F., et al. 2012, ApJ, 756, L25

Deloye, C. J., & Bildsten, L. 2003, ApJ, 598, 1217

Demorest, P. B., Pennucci, T., Ransom, S. M., Roberts, M. S. E., & Hessels, J. W. T. 2010, Nature, 467, 1081

Eichler, D., & Gedalin, M. 1995, in Astronomical Society of the Pacific Conference Series, Vol. 72, Millisecond Pulsars. A Decade of Surprise, ed. A. S. Fruchter, M. Tavani, & D. C. Backer, 235

Ekşİ, K. Y., & Alpar, M. A. 2005, The Astrophysical Journal, 620, 390

Feenberg, E., & Primakoff, H. 1948, Physical Review, 73, 449

Felten, J. E., & Morrison, P. 1963, Physical Review Letters, 10, 453

—. 1966, ApJ, 146, 686

Fermi-LAT Collaboration. 2009a, Science, 325, 848

—. 2009b, ApJ, 697, 1071

Fichtel, C. E., Hartman, R. C., Kniffen, D. A., et al. 1975, ApJ, 198, 163

Fierro, J. M., Arzoumanian, Z., Bailes, M., et al. 1995, ApJ, 447, 807

Flower, P. J. 1996, ApJ, 469, 355

Fortney, J. J., Lodders, K., Marley, M. S., & Freedman, R. S. 2008, ApJ, 678, 1419

Fruchter, A. S., & Goss, W. M. 1992, ApJ, 384, L47

Fruchter, A. S., Gunn, J. E., Lauer, T. R., & Dressler, A. 1988a, Nature, 334, 686

Fruchter, A. S., Stinebring, D. R., & Taylor, J. H. 1988b, Nature, 333, 237

Gentile, P. A., Roberts, M. S. E., McLaughlin, M. A., et al. 2014, ApJ, 783, 69

Giacconi, R., Gursky, H., Kellogg, E., Schreier, E., & Tananbaum, H. 1971, ApJ, 167, L67

Gold, T. 1968, Nature, 218, 731

Gotthelf, E. V., Vasisht, G., Boylan-Kolchin, M., & Torii, K. 2000, ApJ, 542, L37

Halpern, J. P., & Holt, S. S. 1992, Nature, 357, 222

Hartman, R. C., Bertsch, D. L., Bloom, S. D., et al. 1999, ApJS, 123, 79

Hauschildt, P. H., Allard, F., & Baron, E. 1999, ApJ, 512, 377

Hayakawa, S. 1958, Progress of Theoretical Physics, 19, 219

Hessels, J. W. T., Roberts, M. S. E., McLaughlin, M. A., et al. 2011, in American Institute of Physics Conference Series, Vol. 1357, American Institute of Physics Conference Series, ed. M. Burgay, N. D'Amico, P. Esposito, A. Pellizzoni, & A. Possenti, 40–43

Hewish, A., Bell, S. J., Pilkington, J. D. H., Scott, P. F., & Collins, R. A. 1968, Nature, 217, 709

Husser, T.-O., Wende-von Berg, S., Dreizler, S., et al. 2013, A&A, 553, A6

Jackson, B., & Carlberg, J. K. 2012, in AAS/Division for Planetary Sciences Meeting Abstracts, Vol. 44, AAS/Division for Planetary Sciences Meeting Abstracts, 113.16

Kaplan, D. L., Bhalerao, V. B., van Kerkwijk, M. H., et al. 2013, ApJ, 765, 158

Kaplan, D. L., Stovall, K., Ransom, S. M., et al. 2012, ApJ, 753, 174

King, A. R., Davies, M. B., & Beer, M. E. 2003, MNRAS, 345, 678

Kiziltan, B., & Thorsett, S. E. 2010, ApJ, 715, 335

Kluzniak, W., Ruderman, M., Shaham, J., & Tavani, M. 1988, Nature, 334, 225

Komissarov, S. S., & Lyubarsky, Y. E. 2004, MNRAS, 349, 779

Kong, A. K. H., Huang, R. H. H., Cheng, K. S., et al. 2012, ApJ, 747, L3

Kraushaar, W., Clark, G. W., Garmire, G., et al. 1965, ApJ, 141, 845

Kuiper, L., Hermsen, W., Verbunt, F., et al. 2000, A&A, 359, 615

Kulkarni, S. R., Djorgovski, S., & Fruchter, A. S. 1988, Nature, 334, 504

Kulkarni, S. R., & Hester, J. J. 1988, Nature, 335, 801

Landolt, A. U. 1992, AJ, 104, 340

Levinson, A., & Eichler, D. 1991, ApJ, 379, 359

Lorimer, D. R., & Kramer, M. 2004, Handbook of Pulsar Astronomy, ed. R. Ellis, J. Huchra, S. Kahn, G. Rieke, & P. B. Stetson (Cambridge University Press)

Lucy, L. B. 1967, ZAp, 65, 89

Lupton, R. C. 2005, Transformations between SDSS magnitudes and UBVRcIc, `http://www.sdss.org/dr5/algorithms/sdssUBVRITransform.html`

Lynch, R. S., & Bank North Celestial Cap Survey Collaborations. 2013, in IAU Symposium, Vol. 291, IAU Symposium, ed. J. van Leeuwen, 41–46

Manchester, R. N., Hobbs, G. B., Teoh, A., & Hobbs, M. 2005, AJ, 129, 1993

Mann, E. C., Romani, R. W., & Fruchter, A. S. 1999, in Bulletin of the American Astronomical Society, Vol. 31, American Astronomical Society Meeting Abstracts, 1429

Meyers, J. D. 2014, Fermi Gamma-ray Space Telescope, `http://fermi.gsfc.nasa.gov/`

Muñoz-Darias, T., Casares, J., O'Brien, K., et al. 2009, MNRAS, 394, L136

Orosz, J. A., & Hauschildt, P. H. 2000, A&A, 364, 265

Papitto, A., Ferrigno, C., Bozzo, E., et al. 2013, Nature, 501, 517

Patruno, A., Archibald, A. M., Hessels, J. W. T., et al. 2014, ApJ, 781, L3

Pétri, J., & Dubus, G. 2011, MNRAS, 417, 532

Phinney, E. S., Evans, C. R., Blandford, R. D., & Kulkarni, S. R. 1988, Nature, 333, 832

Pilkington, J. D. H., Hewish, A., Bell, S. J., & Cole, T. W. 1968, Nature, 218, 126

Podsiadlowski, P., Rappaport, S., & Pfahl, E. 2001, in Astrophysics and Space Science Library, Vol. 264, The Influence of Binaries on Stellar Population Studies, ed. D. Vanbeveren, 355

Radhakrishnan, V., & Srinivasan, G. 1982, Current Science, 51, 1096

Ramanamurthy, P. V., Bertsch, D. L., Dingus, B. L., et al. 1995, ApJ, 447, L109

Ransom, S. M., Ray, P. S., Camilo, F., et al. 2011, ApJ, 727, L16

Rappaport, S., Joss, P. C., & Webbink, R. F. 1982, ApJ, 254, 616

Ray, P. S., Abdo, A. A., Parent, D., et al. 2012, ArXiv e-prints, arXiv:1205.3089

Reynolds, M. T., Callanan, P. J., Fruchter, A. S., et al. 2007, MNRAS, 379, 1117

Roberts, M. S. E. 2011, in American Institute of Physics Conference Series, Vol. 1357, American Institute of Physics Conference Series, ed. M. Burgay, N. D'Amico, P. Esposito, A. Pellizzoni, & A. Possenti, 127–130

Romani, R. W., Filippenko, A. V., Silverman, J. M., et al. 2012, ApJ, 760, L36

Ruciński, S. M. 1969, Acta Astron., 19, 245

Ruderman, M., Shaham, J., & Tavani, M. 1989a, ApJ, 336, 507

—. 1989b, ApJ, 336, 507

Schlegel, D. J., Finkbeiner, D. P., & Davis, M. 1998, ApJ, 500, 525

Schroeder, J., & Halpern, J. 2014, ArXiv e-prints, arXiv:1401.7966

Sironi, L., & Spitkovsky, A. 2011, ApJ, 741, 39

Srinivasan, G. 1990, Advances in Space Research, 10, 167

Stappers, B. W., Bessell, M. S., & Bailes, M. 1996a, ApJ, 473, L119

Stappers, B. W., Gaensler, B. M., Kaspi, V. M., van der Klis, M., & Lewin, W. H. G. 2003, Science, 299, 1372

Stappers, B. W., Bailes, M., Lyne, A. G., et al. 1996b, ApJ, 465, L119

Steiner, A. W., Lattimer, J. M., & Brown, E. F. 2013, ApJ, 765, L5

Story, S. A., Gonthier, P. L., & Harding, A. K. 2007, ApJ, 671, 713

Strobel, K., & Weigel, M. K. 2001, A&A, 367, 582

Sturner, S. J., & Dermer, C. D. 1994, A&A, 281, L101

Swanenburg, B. N., Bennett, K., Bignami, G. F., et al. 1981, ApJ, 243, L69

The Fermi-LAT Collaboration. 2010, ApJS, 187, 460

—. 2011, ArXiv e-prints, arXiv:1108.1435

The Fermi-LAT collaboration. 2013, ArXiv e-prints, arXiv:1305.4385

Thompson, D. J., Ballet, J., Burnett, T., & Fermi Large Area Telescope Collaboration. 2014, in American Astronomical Society Meeting Abstracts, Vol. 223, American Astronomical Society Meeting Abstracts, 256.01

Thorstensen, J. R., & Armstrong, E. 2005, AJ, 130, 759

Usov, V. V. 1983, Nature, 305, 409

van Hamme, W. 1993, AJ, 106, 2096

van Kerkwijk, M. H., Breton, R. P., & Kulkarni, S. R. 2011, ApJ, 728, 95

van Paradijs, J., Allington-Smith, J., Callanan, P., et al. 1988, Nature, 334, 684

von Zeipel, H. 1924, MNRAS, 84, 665

Wang, Z., Archibald, A. M., Thorstensen, J. R., et al. 2009, The Astrophysical Journal, 703, 2017

Weltevrede, P., Johnston, S., Manchester, R. N., et al. 2010, PASA, 27, 64

Woudt, P. A., Warner, B., & Pretorius, M. L. 2004, MNRAS, 351, 1015

Zhang, L., Fang, J., & Chen, S. B. 2007, ApJ, 666, 1165